Selective Activation of TRPC6 Ion Channel by Metallated Type-B Polyprenylated Polycyclic Acylphloroglucinols

Philipp Peslalz‡[1], Frank Kraus‡[1], Flavia Izzo[1], Anton Bleisch[1], Yamina El Hamdaoui[2], Ina Schulz[2], Andreas M. Kany[3], Anna K. H. Hirsch[3,4], Kristina Friedland*[2], Bernd Plietker*[1]

[1] *Chair of Organic Chemistry, Faculty of Chemistry and Food Chemistry, Technical University Dresden, Bergstr. 66, 01069 Dresden, Germany.*

[2] *Pharm. & Tox. Institut für Biomedizinische und Pharmazeutische Wissenschaften Johannes Gutenberg-Universität Mainz, Mainz, Germany.*

[3] *Helmholtz Institute for Pharm. Research Saarland, (HIPS)–Helmholtz Centre for Infection Research (HZI); Saarbrücken, 66123, Germany.*

[4] *Department of Pharmacy, Saarland University, 66123 Saarbrücken, Germany.*

KEYWORDS Natural product, TRPC, PPAP, calcium, artificial intelligence

ABSTRACT: The selective modulation of TRPC6 ion channels has emerged as a promising therapeutic approach for treating neurodegenerative diseases and depression. Here, we present a significant advancement in this field by demonstrating the selective activation of TRPC6 using a metallated type-B PPAP, designated as **PPAP53**. The success of **PPAP53** is attributed to the utilization of the 1,3-diketone motif present in PPAPs for metal coordination. The metallated PPAPs exhibit water solubility and equipotent activity compared to hyperforin, which is a natural product and considered the gold standard in the field. Notably, and in sharp contrast to type-A PPAPs, type-B PPAPs possess unique properties such as synthetic accessibility in gram scale, facile derivatization, being thermally stable and stable against photochemical oxidation. Our detailed investigations reveal that **PPAP53** selectively binds to the C-terminus of TRPC6. Although cryo electron microscopy has resolved the majority of the TRPC6 structure, the binding site in the C-terminus remained unresolved. To address this issue, we employed state-of-the-art artificial intelligence-based protein structure prediction algorithms, including AlphaFold2, ColabFold, and trRosetta, to predict the missing C-terminus region. Our computational results, validated against experimental data, indicate that **PPAP53** binds to the ^{777}LLKL^{780}-region of the C-terminus, thus providing critical insights into the binding mechanism of **PPAP53** with TRPC6.

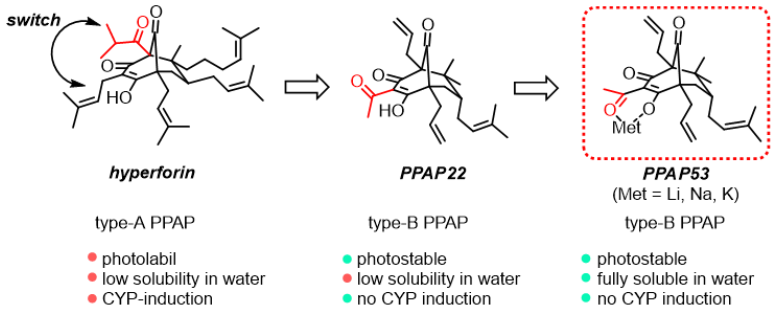

INTRODUCTION

Physiological and pathological processes are strongly regulated by ion channels.[1] These channels are composed of pore-forming proteins that are embedded in the cell membrane[1]. Amongst the different ion channels human transient receptor potential (TRP) proteins are a subclass of 27 different ion channels which can be divided into nine families.[2,3] The TRPC proteins are one of these families and are important for the regulation of Ca^{2+}-flux at the cell membrane of eukaryotes. They are divided into two subfamilies: TRPC1/4/5 and TRPC3/6/7.[4,5] Both subfamilies of TRPCs are discussed as biological targets for treatment of pain, cancer, cardiovascular dysfunction, but also endocrinal, renal and, neuronal diseases, and foster research into the development of selective TRPC-channel agonists or antagonists.[6–9] Importantly, the structure of hTRPC6 has most recently been largely resolved using cryo electron microscopy (cryoEM). (Fig. 1A-C), however, the C-terminus that is part of the inner-cell receptor regulation remained partially unresolved.[10–12]

The TRPC6 channel is a non-selective cation channel that plays a crucial role in regulating the influx of Ca^{2+} across cell membranes. As a result, TRPC6 has been the subject of extensive research efforts in order to understand its function and potential therapeutic applications. Recent studies have identified the extracellular binding sites for TRPC6 agonists AM-0883, M085 and GSK1702934A, which have been found to modulate TRPC6 channel activity (Fig. 1D and E).[11,13]

Hyperforin, a type-A PPAP derivative, can be extracted from the plant *Hypericum perforatum*, commonly known as St. John's Wort.[14,15] It has been known to possess antidepressant properties through its ability to inhibit the reuptake of serotonin andnorepinephrine in neurons.[16] Its antidepressant applications as medicinal products (such as Psychotonin®, Neuroplant®, Hyperforat®) have become increasingly popular. Recent data has shown that hyperforin also elevates intracellular Ca^{2+} concentrations by activating TRPC6 channels, while not activating other TRPC isoforms.[17]

Despite its potential therapeutic benefits, hyperforin has been found to exhibit phototoxicity, cytochrome P450 (CYP) induction properties and being thermally unstable.[18,19] Phototoxicity occurs as a result of the photodynamic generation of singlet oxygen upon exposure to UV radiation,

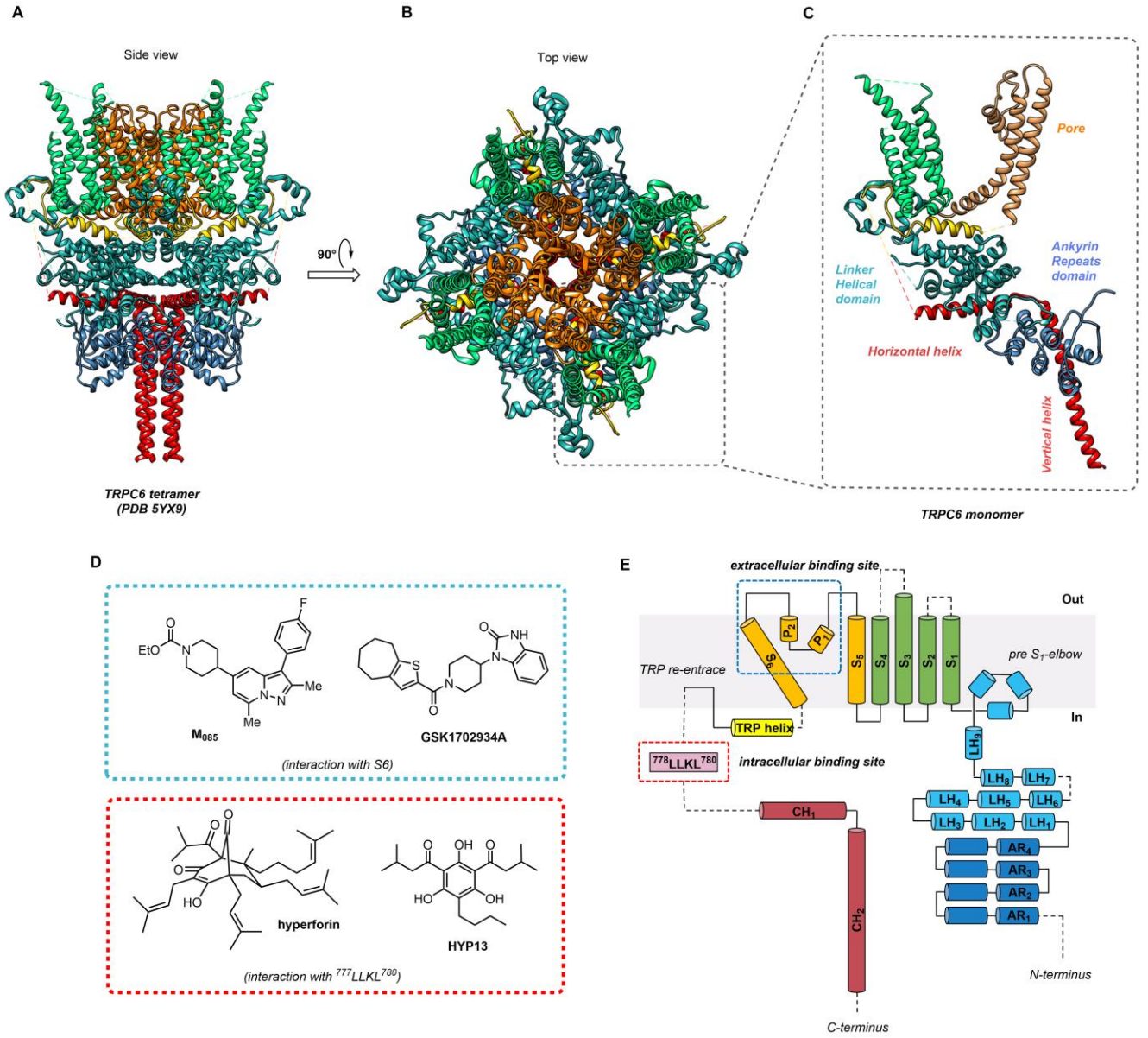

*Figure 1 Cryo-EM structure of hTRPC6 (PDB 5YX9) shown as cartoon. (**A**) hTRPC6 channel is shown in side view. and (**B**) top view revealing the pore. (**C**) Representation of the monomeric structure of hTRPC6. Vertical helix and horizontal helix colored in red, ankyrin repeat domains are colored in blue, linker helical domains in teal, S5 and S6 helix, forming the pore, in orange and S1-S4 in green. Unresolved sequences are indicated with dashed lines (**D**) Literature known TRPC6 agonists that bind extracellular (blue) and intracellular (red) (**E**) Structure of a TRPC6 monomer and domain organization. (Figure adapted from Fig 3. in Ref. 33.),*

resulting in decomposition of the compound and a phototoxic response in the skin. CYP induction leads to an increase in oxidative metabolic reactions and may result in significant drug-drug interactions.[20] These properties present limitations on the therapeutic use of hyperforin. To overcome these limitations, the Friedland group has recently reported that **HYP13** may be a promising candidate for selective TRPC6 activation without the undesired phototoxic and CYP-inducing side-effects.[21]

To this day, natural resources have yielded over 600 members of the PPAP family, exhibiting a broad spectrum of biological activities across various indications.[22] These compounds can be categorized as either type-A or type-B PPAPs, depending on the position of the exocyclic acyl-group (Fig. 2A). [23] Type-A PPAPs, such as hyperforin, are particularly susceptible to light-induced free radical reactions, resulting in a significant increase in oxidation upon exposure to light. It has been proposed that hyperforin reacts with $^1O_2$ by undergoing an intramolecular cyclization, forming furohyperforin hydroperoxide, followed by the elimination of hydrogen peroxide (Fig. 2B). [24] Moreover, it has been suggested that St. John's wort produces hyperforin to act as a radical scavenger for the photosensitizer hypericin.[25]

We were actively engaged in the total synthesis of type-B PPAPs, as well as the systematic modification of the common [3.3.1]bicyclononatrione-core for medical applications, including as antimicrobial compounds.[26–31] Given that hyperforin has been reported to possess potent antimicrobial properties, it was hypothesized that type-B PPAPs may also exhibit similar activities in other medical indications.[32]

In this study, we demonstrate that metallated derivatives of **PPAP22** are potent and selective TRPC6-activators. Through detailed experimental studies, it was revealed that the mode of action is similar to hyperforin or **HYP13**, through binding to the ^{777}LLKL^{780}-region of the C-terminus. Notably, our compounds are photostable and highly water-soluble. In terms of its own metabolism, **PPAP53** showed moderate murine metabolic and plasma stability (MLM $t_{1/2}$ 31.5 ± 4.9 min, Cl_{int} 44.7 ± 7.2 µL/mg/min; plasma $t_{1/2}$ 154 ± 53 min). Additionally, photostability tests of **PPAP53** confirmed the long-term stability to light and oxygen.

Predictive protein algorithms such as trRosetta were utilized to predict the unresolved parts within the C-terminus and were aligned with the cryoEM-structure, yielding a TM-score of 0.94. Subsequent docking studies were cross-referenced with the experimental data, further supporting the ^{777}LLKL^{780}-region of the C-terminus as the binding site of **PPAP53**.

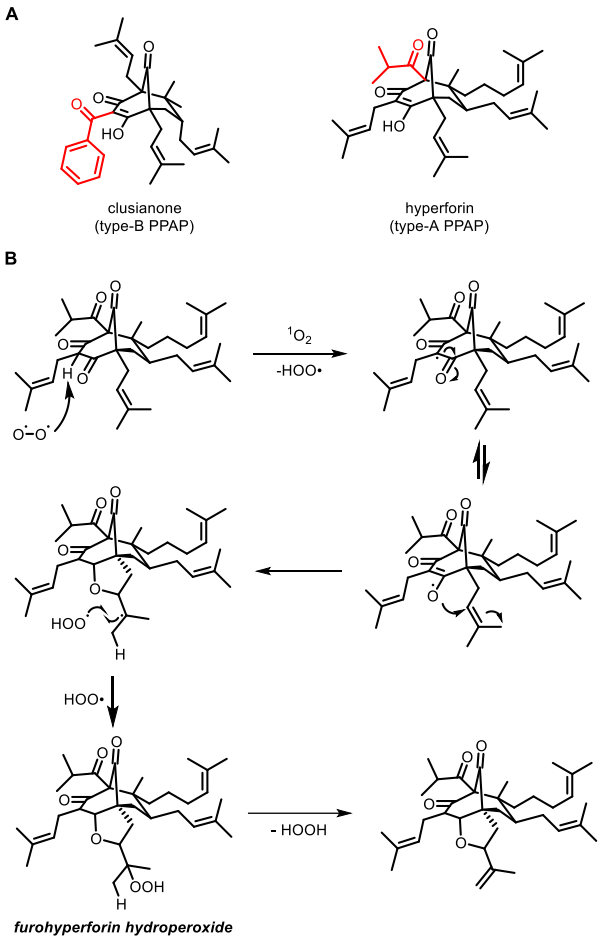

Figure 2 (A) Representative type-A and type-B PPAP natural products. (B) Radical induced cyclisation of hyperforin to furohyperforin hydroperoxide and coupled release of hydrogenperoxide.

RESULTS AND DISCUSSION

The current investigation was initiated through a comprehensive screening of various derivatives of PPAPs, which had previously been reported to possess potent antibiotic properties.[26]

These compounds were evaluated for their ability to induce Ca^{2+} influx in PC12 cells using the FLIPR Calcium 4 assay. The induction of Ca^{2+} influx is indicative of potential TRPC activity.[17,33] Of all compounds tested, **PPAP22** elicited a relatively modest increase in intracellular Ca^{2+} in PC12 cells at a concentration of 10 µM (Fig. 4A), while hyperforin robustly induce Ca^{2+} increase and activate TRPC6 channels at a concentration of 10 µM, with EC_{50} values for TRPC6 activation of 1 µM.[34]

Concentrations higher than 10 µM are considered to be toxic.[21] One potential explanation for this lower activity is the low solubility of lipophilic **PPAP22**. To enhance the water-solubility and bioavailability of **PPAP22** without altering its overall structure, we sought to utilize the PPAP's inherent 1,3-dicarbonyl motif as a potential bidentate ligand to metal cations. Treatment of type-B PPAPs with alkaline bases led to the clean formation of metallated **PPAP53**, **PPAP60** and **PPAP61** (starting from **PPAP22**) (Fig. 3B). Subsequent testing for Ca^{2+}-influx stimulation revealed that all of the metallated PPAPs exhibit good levels of activity, with **PPAP53** surpassing the Ca^{2+}-influx stimulation of hyperforin (Fig. 4B). The improvement of solubility could be confirmed as kinetic solubility of **PPAP53** was determined to be >200 µM, while the solubility of **PPAP22** was 49.1 ± 8.6 µM in 1% DMSO/PSB.

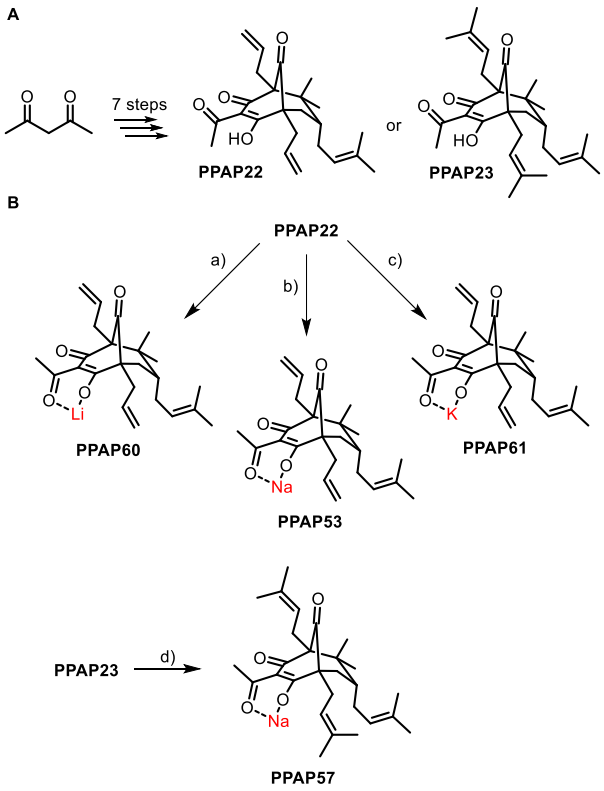

*Figure 3 Synthesis of PPAP metal salts. (A) Synthetic route to access **PPAP22** and **PPAP23**. (B) Metallation of **PPAP22** and PPAP23 under following reaction conditions: a) n-BuLi, THF, 0°C, 1h, b) NaH, THF, 0°C, 1h, c) KH, THF, 0°C, 1h, d) NaH, THF, 0°C, 1h*

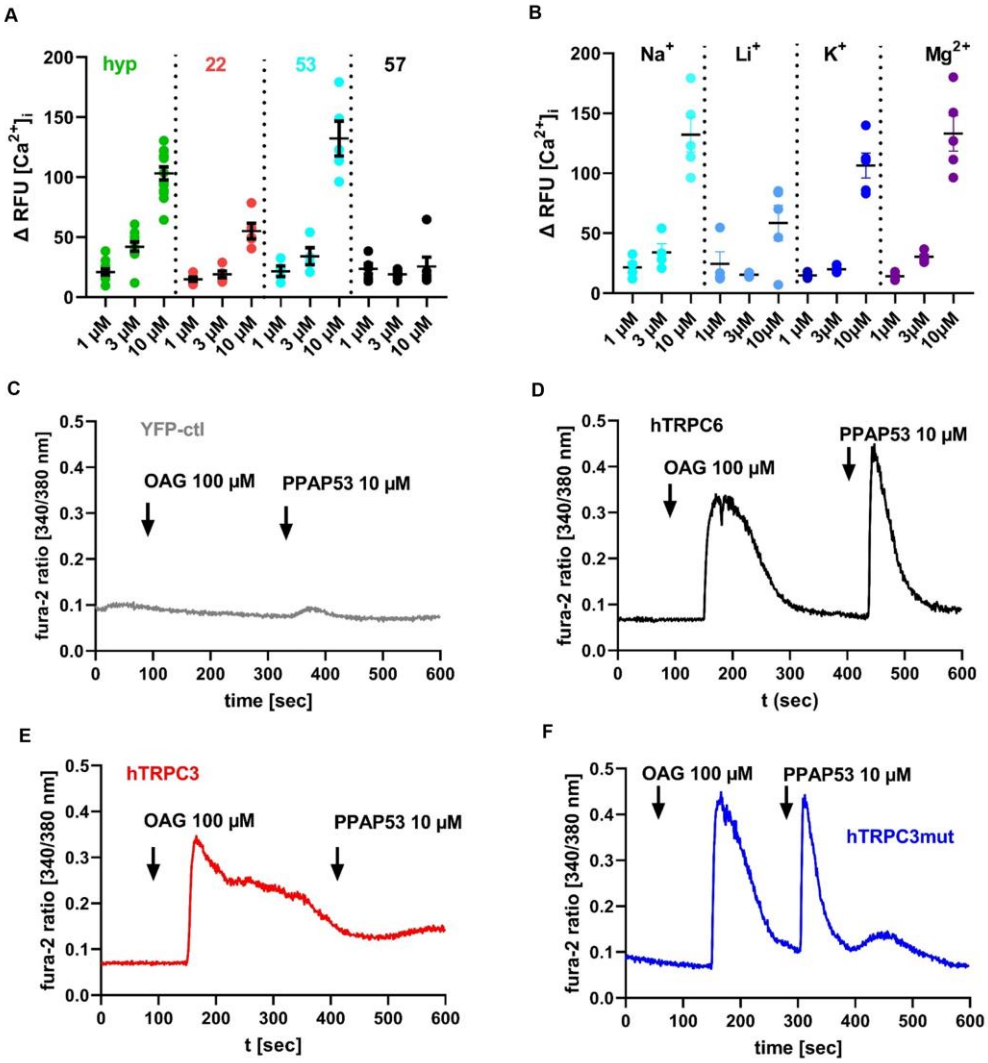

*Figure 4 (**A**) (**B**) Effect of PPAPs on [Ca^{2+}] in PC12 cells and HEK293 cells expressing human TRPC channels using the FLIPR Calcium-6 AM Assay. Cells were stimulated with increasing concentrations from 1 – 10 µM. As internal control, hyperforin (hyp) was used. (n = 4 – 6 biological independent experiments). Single cell Ca^{2+} imaging was conducted in HEK293 cells transiently expressing pcDNA3.1 plasmid vector with DNA coding (**C**) only for eYFP (ctl, white), (**D**) hTRPC6 (black), (**E**) hTRPC3mut (red), or (**F**) hTRPC3mut (blue) all expressed as C-terminal eYFP fusion proteins. Cells were stimulated with the solvent DMSO (0.1 %), OAG (100 µM) or **PPAP53** (10 µM) and intracellular Ca^{2+} alterations were detected using fura-2 AM (n = 3 independent biological experiments). Cells were selected according to their eYFP fluorescence and their OAG sensitivity. Representative time traces were monitored in HEK293 cells stimulated with OAG (100 µM) 60 sec after starting the experiment and after 300 sec **PPAP53** (10 µM) was applied.*

To further investigate the mode of action, the effect of **PPAP53** was tested in HEK293 cells transiently expressing YFP-tagged TRPC3 and TRPC6 channels (Fig. 4C-E).[21] Single cell calcium measurements were conducted using the fluorescence dye fura-2, by applying hyperforin (10 µM) or the analogue OAG of the endogenous unselective TRPC3/6/7 activator diacylglycerol. In TRPC6- and TRPC3-expressing cells, application of OAG resulted in a rapid increase in [Ca^{2+}], reflected by an increase in the fura-2 ratio. In contrast, hyperforin (10 µM) only induced an increase in the fura-2 ratio in TRPC6-expressing cells. **PPAP53** (10 µM) also only induced a significant increase in the fura-2 ratio in TRPC6-expressing HEK293 cells.

To further elaborate on the similarity of binding sites between hyperforin and **PPAP53** at hTRPC6, a recently described mutant of TRPC6 was used.[21] Hyperforin is known to bind at the motif ^{777}LLKL^{780} in the C-terminal region of hTRPC6, which was not resolved in recent cryo-EM structures. This motif differs from the closely related hTRPC3 and hTRPC7 channels by the corresponding amino acids ^{708}IMRI^{711} of hTRPC3 and ^{722}IMRI^{725} of hTRPC7. Therefore, the ^{777}LLKL^{780} motif from TRPC6 was implemented into TRPC3 demonstrating that hyperforin is now able to also activate the mutated ^{708}LLKL^{711} hTRPC3 channel (FIG 4F). Again, **PPAP53** showed similar effects as hyperforin. These results suggest that hyperforin and **PPAP53** might share the same binding site at TRPC6 channels.

In order to rationalize the experimental findings and investigate the binding motif of hyperforin and **PPAP53** at TRPC6, in silico experiments were conducted. The traditional method for this involves docking ligands to protein structures that have been determined through techniques such as crystallography or microED, cryoEM, etc. Despite the availability of various hTRPC6-structures, the probable

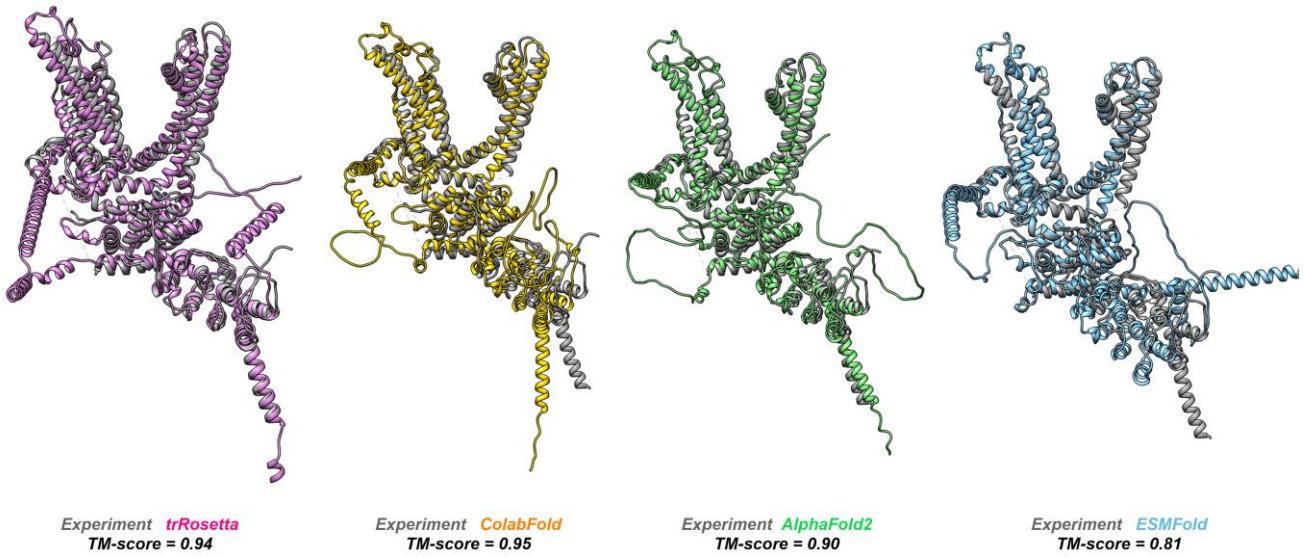

Figure 5 Superposition of the cryoEM structure of hTRPC6 monomer (PBD 5YX9) (grey) with the TRPC6 model generated with trRosetta (pink), ColabFold (yellow), AlphaFold2 (green) and ESMFold (blue). The structural similarities are ranked by the calculated TM-scores for each model.

binding site of PPAPs has not been resolved in the literature. [11,12,35,36] Unresolved positions in the TRPC6 channel can be found in the N-terminus (residues 1-84), between AR3 and AR4 (residues 193-203), between the linker helix 6 and 7 (residues 350-357), between the S1 and S2 helix (residues 464-491), between the S3 and S4 helix (residues 560-585), between the TRP reentrant and the C-terminal helix 1 (residues 767-852), and at the end of the C-terminus (residues 922-931). In light of this, we employed the use of artificial intelligence (AI) based algorithms to overcome the lack of structural data within these relevant regions of the receptor structure (Fig. 6). Different AI algorithms were utilized to predict the tertiary structure from the amino acid sequence of the full-length protein, in order to study the potential binding site and the results were validated by comparison with experimental results (Fig. 5).[37–43]

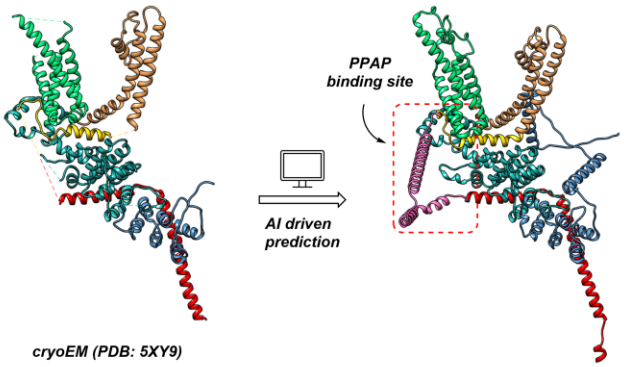

Figure 6 Completion of the unresolved areas from the cryoEM structure by the use of protein structure prediction algorithms.

AlphaFold2 (AF2) predicts the topology of transmembrane (TM) proteins highly accurately.[44] The pLDDT (predicted Local Distance Difference Test) confidence measure predicts the accuracy of the Cα Local Distance Difference Test (lDDT-Cα) for the corresponding prediction. Even though the predicted AF2-TRPC6 model shows high plDDT values the model lacks of confidence in the region where the hypothesized binding site is located. A faster and accelerated prediction of protein structures and complexes offers the lately published AI-driven algorythm ColabFold (CF) by combining the fast homology search of MMseqs2 with AlphaFold2. [45] The predicted three-dimensional structure CF-TRPC6 has slightly higher plDDT values than AF2-TRPC6 but still has problems to resolve the domains that are already unresolved in the corresponding crystal structure.

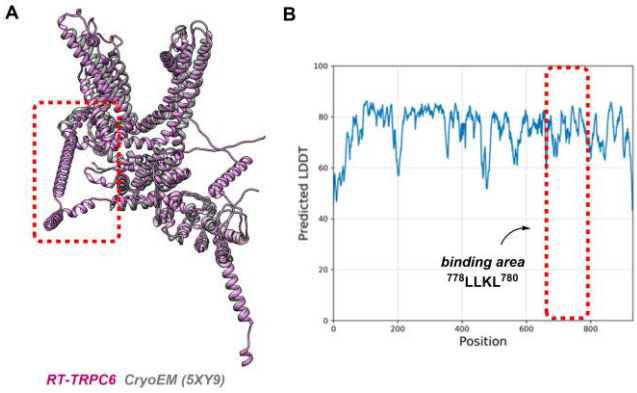

*Figure 7 (**B**) Prediction of the 3D-strucuter of hTRPC6 monomer with trRosetta (RT-TRPC6) and superposition with the corresponding cryoEM structure (PDB: 5YX9). (**C**) Evaluation of pLDDT values within the binding site.*

Additionally, TRPC6 structures were generated using trRosetta (RT) with enabled template search, a web-based platform for fast and accurate protein structure prediction, powered by deep learning and Rosetta.[46] RT-TRPC6 shows high confidence within the overall predicted structure. Even the more flexible domains that are not resolved in the cryoEM structure are predicted with high plDDT values (Fig. 7B). To confirm the structural accuracy of the predicted

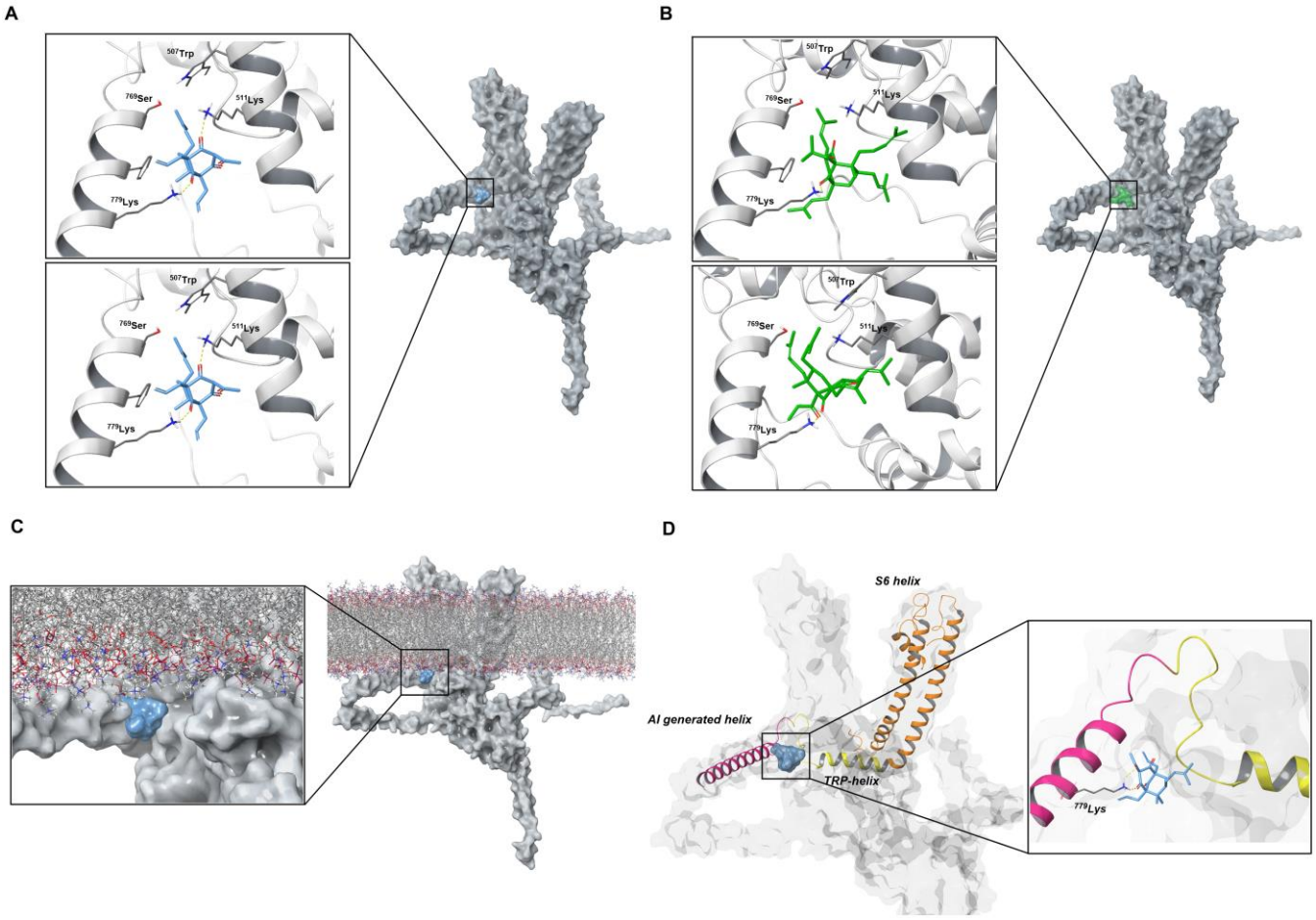

*Figure 8 Binding mode of PPAPs within RT-TRPC6 monomer (**A**) Docking pose of both PPAP53 isomers (blue) within RT-TRPC6 .(**B**) Docking pose of both hyperforin isomers (green) within RT-TRPC6 (**C**) RT-TRPC6 embedded in a membrane model with docked **PPAP53** (**D**) Visual representation **PPAP53** docked to the AI-generated helix connected over the TRP-helix to S6*

monomer RT-TRPC6 was compared to the monomer of the known cryoEM structure (PDB 5YX9) (Fig. 7A). [36] The superposition of the cryoEM structure and the predicted structure is validated by the global superposition metric template modelling score (TM-score).[47] In our case the superposition of hTRPC6 and the predicted structure RT-TRPC6 generates a TM-score of 0.94, indicating high structural similarity (Fig. 5).

The newly predicted C-terminus part (Fig. 6 in pink) in RT-TRPC6, in which the hypothesized binding site is located, is shown as a long helical structure. Previous data showed that CD spectra of isolated TRPC6 peptides carrying the ^{777}LLKL^{780} motif revealed an α-helical structure in the absence and presence of hyperforin, which is consistent with the predicted model.[21]

In order to gain an understanding of the potential binding pose of the predicted monomer, molecular docking experiments were performed using energy-minimized structures of **PPAP53** and hyperforin. Hydrogen atoms were added and different protonation states and ionization states for each ligand were generated for a pH range of 7.0 ± 2. The preparation of the ligands resulted in the generation of two states per ligand, in which the exocyclic acyl group of **PPAP53** or the exocyclic isoprenyl chain of hyperforin can undergo keto-enol driven conversion in stereochemical orientation. Thes results are consistent with ^{1}H-NMR data showing the enol form of PPAPs in acidic solvents like chloroform, which get suppressed in neutral solvents like DMSO.

Docking studies indicate that both isoforms bind to the same region, which is located in the AI-predicted alpha-helical domain connected to the TRP-helix, forming a cave-like structure directly underneath the cell membrane (Fig. 8. C). The regions missing in the cryoEM structure are likely to be highly mobile.

In order to determine the structural interactions of the ligand with the AI-predicted domain, we employed an induced fit docking approach and analyzed the structural interaction fingerprints (SIFt). The SIFt analysis of over 50 different docking poses indicated that the residues located on the AI-predicted motif, the TRP-domain, and the S2 region were primarily responsible for mediating the binding of PPAPs. This tool identifies amino acid residues that exhibit polar or non-polar, aromatic, hydrophobic interactions, and hydrogen bond interactions with the docking poses or are situated in close proximity (within 10Å) to the ligand. The SIFt revealed that 511Lys, 514Trp, 515Thr, 772Ser, 775Tyr, 776Leu and 779Lys were the main residues showing >75% involvement in all poses.

The docking studies with RT-TRPC6 are in agreement with experimental data, revealing the binding situation involving 779Lys within the predicted sidechain and 511Lys within

S2 (Fig.8 A and B). The binding site is directly connected via the TRP-helix to the transmembrane helix S6, which could be stimulated by ligand binding and induce Ca^{2+} influx (Fig. 8D). It is hypothesized that the movement of S6 stimulates tilting and downward movement of S1 to S4 from adjacent subunits, resulting in a rotation around the central ion-permeable pathway and opening of the pore channel.[14]

The docked PPAPs were found to be located close to 783Trp, which was previously utilized to identify the binding site of hyperforin. Tryptophan fluorescence is highly sensitive to changes in the environment, such as hydrophobicity, and can therefore provide information about ligand binding. The ascending titration of hyperforin (1-50µM) showed a stronger fluorescence intensity in a native TRPC6 peptide compared to a mutant TRPC6 peptide with the sequence IMRI instead of ^{777}LLKL^{780}.[21]

The results of our docking simulations are consistent with experimental data and provide insight into the binding situation of **PPAP53** and hyperforin with RT-TRPC6.

CONCLUSION

In conclusion we developed new water soluble metallated unnatural type-B PPAPs which selectively activate TRPC6. We could demonstrate that metallated unnatural type-B PPAPs induce a higher Ca^{2+}-influx in PC12 cells compared to hyperforin, eliminating any disadvantages of hyperforin, such as light instability, air instability, CYP-induction and complicated synthesis work. Mutation studies showed that **PPAP53** binds to the ^{777}LLKL^{780} motif similar to hyperforin, which is not resolved in cryoEM structures. To overcome the lack of information AI-generated models of TRPC6 were used to identify a new intracellular binding site for type-B PPAPs *in silico* that aligns well with experimental findings. These findings help to rationalize the binding mechanism of PPAPs within TRPC6 channels and open the field for the development of more potent unnatural type-B PPAPs.

MATERIAL AND METHODS

All reactions and manipulations which are sensitive towards air or moisture were performed under dry argon by using standard Schlenk techniques. All solvents were purified prior to use. All chemicals were purchased from Acros Organics, Sigma Aldrich, Alfa Aesar, TCI or ChemPUR. NMR spectra were recorded on a Bruker Avance 300 spectrometer at 300 MHz (^{1}H-NMR), 75 MHz (^{13}C-NMR), a Bruker Ascend 400 spectrometer at 400 MHz (^{1}H NMR), 376 MHz (^{19}F-NMR), 101 MHz (^{13}C-NMR), a Bruker Avance 500 spectrometer at 500 MHz (^{1}H-NMR), 126 MHz (^{13}C-NMR), 202 MHz (^{31}P-NMR) or a Bruker Avance 700 spectrometer at 700 MHz (^{1}H-NMR), 176 MHz (^{13}C-NMR). Coupling constants J are given in Hz. The following abbreviations are used in the analysis of NMR spectra: s = singlet, d = doublet, t = triplet, q = quartet, hept = heptet, sept = septet, snr = broad singlet. Combination of these abbreviations are applied whenever more than one coupling is observed. IR spectra were measured on a FT-IR spectrometer in an ATR mode. The intensity of the observed peaks is given in parenthesis: s = strong, m = medium, w = weak. Mass spectra were measured using electrospray ionization on a Bruker micrOTOF-Q. High performance liquid chromatography (HPLC) was performed using a Knauer K-501 pump, Knauer RI-detector K 2400 and a Macherey- Nagel VP250/21 Nucleodur 100-5 column.

Cell culture and transfection of HEK293 cells

Human embryonic kidney (HEK 293) cells were cultured in Dulbecco's Modified Eagle Medium (DMEM; ThermoFisherScientific, Darmstadt, Germany; #41965039) supplemented with 10% heat-inactivated Fetal Bovine Serum (FCS; ThermoFisherScientific, Darmstadt, Germany; #10500-064) and 10 mM penicillin/streptomycin (Pen-Strep; ThermoFisherScientific, Darmstadt, Germany; #15140122) at 37°C. For Transfection, HEK 293 cells were grown on poly-L-lysine (Sigma-Aldrich, Taufkirchen, Germany; #P2636) coated glass coverslips in 6-well plates with a density of 0,1 x 106 cells per well for Single-Cell Calcium Imaging and Western Blot and with a density of 0,5 x 105 cells for electrophysiological measurements. After 24 h, media was exchanged and cells were transfected transiently with a transfection cocktail containing 0.5 to 1 µg DNA, 2 µL Effectene (Qiagen, Hilden, Germany; #301425) transfection reagent and 50 µL Opti-MEM (ThermoFisherScientific, Darmstadt, Germany; #51985034) medium.

Single cell calcium imaging in HEK293 cells

[Ca^{2+}]-measurements in HEK293 cells were carried out using the fluorescence indicator fura-2-acytoxymethyl ester (Fura 2-AM; ThermoFisherScientific, Darmstadt, Germany; #F1201) combined with a monochromator–based imaging system (T.I.L.L. Photonics; FEI, Gräfeling, Germany) attached to a fluid immersion objective (LUMPLFLN 40XW/0.80 w). Cells were loaded with a cocktail composed of 2,5 µM Fura 2-AM, 0,01% pluronic-F127 (ThermoFisherScientific, Darmstadt, Germany; #P6866) for 30 minutes at room temperature (22-24 °C) in a standard Hank's Balanced Salt Solution (HBSS) buffer composed of 138 mM NaCl, 6 mM KCl, 1 mM MgCl2, 1 mM $CaCl_2$ and 10 mM HEPES ([4-(2-hydroxyethyl)-1-piperazineethanesulfonic acid]) adjusted to pH 7.4 with NaOH at room temperature. Afterwards, cells were washed with HBSS and left for another 30 min at RT in HBSS. Cover slips were then mounted in a bath chamber made of plexiglas on the stage of the microscope (Olympus BX51WI, Hamburg, Germany). Ca^{2+} influx was recorded and visualized in TillVision Live Acquisition and Offline Analysis software [formerly FEI Munich GmbH (Till Photonics), now Thermo Fisher Scientific] as a ratio of 340/380nm with a 40 x objective. Ca^{2+}-bound Fura2-AM is excitable at 340 nm and the unbound state of Fura2-AM at 380 nm. The ratio was calculated by analyses of emission which was detectable at 510 nm after excitation with each wavelength.

Cell culture and FLIPR Calcium-6 AM assay in PC12 cells

PC12 cells were cultured in DMEM (ThermoFisherScientific, Darmstadt, Germany; #41965039) supplemented with 10% heat-inactivated fetal calf serum (ThermoFisherScientific, Darmstadt, Germany; #10500-064) and 5% heat-inactivated horse serum , 50 U/mL penicillin, and 50µg/mL streptomycin (Pen-Strep; ThermoFisherScientific, Darmstadt, Germany; #15140122) at 37°C in a humidified incubator containing 5% CO_2. 24h before FLIPR Calcium-6 AM Assays were initiated, 50.000 cells per well were plated in 96 well plates in 100 µL DMEM. 24h after seeding, DMEM with

growth factors was replaced by 100 µL DMEM without growth factors. Calcium-6 AM (Molecular Devices, #R8191) was added as described by the manufacturer protocol in 100 µL Hank's balanced standard solution composed of 138 mM NaCl, 6 mM KCl, 1 mM $MgCl_2$, 1 mM $CaCl_2$, 5.5 mM glucose, and 10 mM HEPES (adjusted to pH 7.4 with NaOH). After 2 h incubation, experiments were run at the Flex station 3. Calcium 6-AM was excited at 485 nm and the emission was measured at 515 nm. The compounds were applied in 50 µL HBSS. Baseline [Ca^{2+}] was measured for 200 sec, the respective compound (dissolved in 0.1 . 1 % DMSO) was added and change in fluorescence was measured for 800 sec. As positive controls, hyperforin (10 µM, kindly provided by Dr. Willmar Schwabe, Karlsruhe) or KCl (80 mM) were used.

General Procedure for the synthesis of PPAP metal salts
In a heated 5 ml finger schlenk under Ar-atmosphere, 1.0 eq. of **PPAP22** or **PPAP23** (previously described)[26] was dissolved in dry THF (1.0 M) and treated with the corresponding metal source (1.0 eq.) at 0°C if not stated otherwise. The resulting solution was stirred for one hour at room temperature. After completion (monitoring via TLC), the solution was layered with n-pentane, the precipitation filtered off and washed with n-pentane.

PPAP53
According to general procedure, **PPAP22** (77 mg, 0.2 mmol, 1.0 eq.) was treated with NaH (60% in mineral oil, 8.0 mg, 0.2 mmol, 1.0 eq.) to yield **PPAP53** as a white powder (49.6 mg, 0.12 mmol, 61%).
^{1}H-NMR (D^2O, 600 MHz): δ = 5.64 (ddt, J = 16.8, 10.4, 6.4 Hz, 1H), 5.41 (ddt, J = 16.8, 10.4, 6.3 Hz, 1H), 5.07 – 4.81 (m, 5H), 3.65 (ddd, J = 6.7, 4.2, 2.5 Hz, 1H), 2.49 (t, J = 10.6 Hz, 2H), 2.35 (d, J = 6.5 Hz, 2H), 2.15 (s, 3H), 2.01 – 1.91 (m, 2H), 1.83 – 1.75 (m, 1H), 1.57 (s, 3H), 1.42 (s, 3H), 1.08 (s, 2H), 0.82 (s, 2H) ppm. ^{13}C-NMR (D_2O, 151 MHz): δ = 216.4, 203.6, 193.0, 192.9, 135.3, 135.0, 133.7, 124.9, 122.1, 117.1, 116.7, 67.7, 60.7, 47.6, 45.7, 39.2, 36.0, 30.6, 30.5, 28.8, 26.1, 24.9, 22.2, 17.2 ppm. IR (Film): ν (cm-1) = 2973 (w), 2924 (w), 2873 (w), 2055 (w), 2030 (w), 2009 (w), 1711 (w), 1641 (s), 1579 (s), 1533 (s), 1473 (w), 1454 (m), 1368 (s), 1341 (s), 1198 (m), 1136 (w), 1064 (w), 996 (w), 912 (s), 881 (w). HRMS (ESI neg, $C_{24}H_{31}O_4Na$) calculated ([M - Na]-): 383.2228; found: 383.2234

PPAP61
According to general procedure, **PPAP22** (26.9 mg, 0.07 mmol, 1.0 eq.) was treated with KH (2.8 mg, 0.07 mmol, 1.0 eq.) to yield **PPAP61** as a pale yellow powder (20.8 mg, 0.05 mmol, 71%).
^{1}H-NMR (D_2O, 600 MHz) δ = 5.64 (ddt, J = 16.9, 10.4, 6.4 Hz, 1H), 5.42 (ddt, J = 17.0, 10.5, 6.4 Hz, 1H), 5.05 – 4.82 (m, 5H), 2.59 – 2.46 (m, 2H), 2.36 (d, J = 6.4 Hz, 2H), 2.24 – 2.17 (m, 2H), 2.16 (s, 3H), 2.15 – 2.09 (m, 2H), 1.98 (dt, J = 14.3, 10.8 Hz, 2H), 1.58 (s, 3H), 1.45 (dd, J = 10.5, 5.0 Hz, 1H), 1.43 (s, 3H), 1.10 (s, 3H), 0.84 (s, 3H) ppm. ^{13}C-NMR (DMSO-d_6, 151 MHz,) δ = 217.50, 201.63, 194.95, 193.51, 142.04, 136.00, 130.95, 124.13, 121.89, 121.10, 71.14, 65.12, 51.37, 50.38, 42.10, 41.83, 37.09, 36.96, 33.91, 32.03, 30.90, 27.78, 22.87 ppm. IR (Film): ν (cm-1) = 2973 (w), 2924 (w), 2873 (w), 2055 (w), 2030 (w), 2009 (w), 1711 (w), 1641 (s), 1579 (s), 1533 (s), 1473 (w), 1454 (m), 1368 (s), 1341 (s), 1198 (m), 1136 (w), 1064 (w), 996 (w), 912 (s), 881 (w). HRMS (ESI neg, $C_{24}H_{31}O_4K$) calculated ([M - K]-): 383.2228; found: 383.2236.

PPAP60
According to general procedure, **PPAP22** (19.2 mg, 0.05 mmol, 1.0 eq.) was treated with n-BuLi (2.5 M in n-hexane, 20µl, 0.05 mmol, 1.0 eq.) at -78°C to yield **PPAP60** as a white powder (11.6 mg, 0.03 mmol, 59%).
^{1}H-NMR (MeOD, 600 MHz): δ = 5.96 – 5.84 (m, 1H), 5.65 – 5.54 (m, 1H), 5.13 – 4.93 (m, 5H), 2.72 – 2.58 (m, 2H), 2.57 – 2.46 (m, 2H), 2.35 – 2.24 (m, 1H), 2.32 (s, 3H), 2.24 – 2.15 (m, 1H), 2.12 – 2.02 (m, 2H), 1.70 (s, 3H), 1.54 (s, 3H), 1.48 – 1.41 (m, 1H), 1.27 (s, 3H), 0.98 (s, 3H) ppm. ^{13}C-NMR (MeOD, 151 MHz): δ = 216.4, 203.6, 193.0, 192.9, 135.3, 135.0, 133.7, 124.9, 122.1, 117.1, 116.7, 67.7, 60.7, 47.6, 45.7, 39.2, 36.0, 30.6, 30.5, 28.8, 26.1, 24.9, 22.2, 17.2 ppm. IR (Film): ν (cm-1) = 2974 (m), 2926 (m), 2877 (m), 2179 (w), 2152 (w), 2039 (w), 1977 (w), 1725 (m), 1663 (m), 1638 (s), 1576 (s), 1530 (s), 1430 (s), 1372 (s), 1132 (m), 1072 (m), 1000 (m), 915 (s), 839 (m), 680 (w), 636 (m), 568 (w), 516 (m).
HRMS (ESI neg, $C_{24}H_{31}O_4Li$) calculated ([M - Li]-): 383.2228; found: 383.2233.

PPAP57
According to general procedure, **PPAP23** (79.0 mg, 0.18 mmol, 1.0 eq.) was treated with NaH (60% in mineral oil, 8.0 mg, 0.2 mmol, 1.1 eq.) at 0°C to yield **PPAP57** as a white powder (42.6 mg, 0.03 mmol, 59%).
^{1}H-NMR (D_2O, 300 MHz): δ = 5.61 – 5.46 (m, 1.7H), 5.46 – 5.30 (m, J = 15.2 Hz, 0.6H), 5.21 – 5.06 (m, J = 18.1, 10.9 Hz, 1H), 5.07 – 4.95 (m, 1.4H), 2.53 (d, J = 4.2 Hz, 2H), 2.37 (d, J = 5.4 Hz, 2H), 2.31 – 2.12 (m, 6H), 2.04 (s, 2H), 1.67 (s, 6H), 1.65 – 1.54 (m, 6H), 1.52 (s, 6H), 1.17 (s, 3H), 0.90 (s, 3H) ppm. ^{13}C-NMR (D_2O, 151 MHz): δ = 201.0, 200.0, 199.5, 194.1, 134.7, 134.3, 133.1, 130.1, 129.6, 128.3, 127.2, 126.8, 126.1, 125.4, 125.2, 123.8, 123.5, 119.8, 119.4, 118.9, 114.8, 69.1, 66.2, 64.3, 59.9, 48.7, 48.6, 48.2, 46.3, 39.7, 31.0, 29.4, 29.3, 28.3, 27.9, 26.9, 26.7, 26.6, 26.5, 26.0, 26.0, 25.9, 25.6, 22.1, 22.0, 18.2, 18.1, 18.0, 17.9, 17.8 ppm. IR (Film): ν (cm-1) = 2967 (m), 2918 (m), 1714 (m), 1643 (s), 1576 (s), 1535 (s), 1435 (s), 1367 (w), 1341 (w), 1144 (w), 1107 (m).1073 (w), 972 (m), 879 (w), 838 (m). HRMS (ESI neg, $C_{28}H_{40}O_4Na$) calculated ([M – Na]-): 439.6165; found: 439.6172.

Kinetic Turbidimetric Solubility
The desired compounds were sequentially diluted in DMSO in a 96-well plate. 1.5 µL of each well were transferred into another 96-well plate and mixed with 148.5 µL of PBS. Plates were shaken for 5 min at 600 rpm at room temperature (r.t.), and the absorbance at 620 nm was measured. Absorbance values were normalized by blank subtraction and plotted using GraphPad Prism 8.4.2 (GraphPad Software, San Diego, CA, USA). Solubility (S) was determined based on the First X value of AUC function using a threshold of 0.005.

Metabolic Stability in Liver Microsomes
For the evaluation of phase I metabolic stability, the compound (1 µM) was incubated with 0.5 mg/mL pooled mouse liver microsomes (Xenotech, Kansas City, USA), 2 mM

NADPH, 10 mM MgCl2 at 37 °C for 120 min on a microplate shaker (Eppendorf, Hamburg, Germany). The metabolic stability of testosterone, verapamil and ketoconazole were determined in parallel to confirm the enzymatic activity of mouse liver microsomes. The incubation was stopped after defined time points by precipitation of aliquots of enzymes with 2 volumes of cold acetonitrile containing internal standard (15 nM diphenhydramine). Samples were stored on ice until the end of the incubation and precipitated protein was removed by centrifugation (15 min, 4 °C, 4,000 g). Concentration of the remaining test compound at the different time points was analyzed by HPLC-MS/MS (TSQ Quantum Access MAX, Thermo Fisher, Dreieich, Germany) and used to determine half-life (t1/2).

Stability in Plasma

To determine stability in mouse plasma, the compound (1 µM) was incubated with pooled CD-1 mouse plasma (Neo Biotech, Nanterre, France). Samples were taken at defined time points by mixing aliquots with 4 volumes of acetonitrile containing internal standard (12.5 nM diphenhydramine). Samples were stored on ice until the end of the incubation and precipitated protein was removed by centrifugation (15 min, 4 °C, 4,000 g, 2 centrifugation steps). Concentration of the remaining test compound at the different time points was analyzed by HPLC-MS/MS (TSQ Quantum Access MAX, Thermo Fisher, Dreieich, Germany). The plasma stability of procain, propantheline and diltiazem were determined in parallel to confirm the enzymatic activity.

Photostability

According to Ang et al.[48] two portions of **PPAP53** (5.0 mg) were dissolved in a solvent mixture of aqueous ammonium acetate buffer and methanol (1:7, 8 mL each) and one was set to pH = 2 with formic acid and the other one was kept at neutral pH. Both mixtures were irradiated with sunlight under air for one week. The solvent was concentrated in vacuo to one third of the original volume and then extracted with ethyl acetate (3 x 10 mL), dried over Na_2SO_4, filtered and concentrated in vacuo. The crude spectra showed no decomposition and the material was recovered quantitatively.

Protein structure prediction of TRPC6 and TRPC3 Ion Channels

hTRPC6 (Q9Y210) and hTRPC3 (Q13507) protein sequences were obtained from the UniProt database (https://www.uniprot.org/, accessed date: 01 August 2022). AlphaFold2[37,49], ColabFold[45], trRosetta[46] and EMSFold[40] were used with default settings to generate predicted models of hTRPC6 and hTRPC3 monomer. Models were visualized with Maestro (Schrödinger Release 2022-4: Maestro, Schrödinger, LLC, New York, NY, 2022).[50] Each prediction generated five models which were overlayed with the corresponding crystal structure (PDB: 5YX9 for hTRPC6 and PDB: 5ZBG for hTRPC3) in Pymol (The PyMOL Molecular Graphics System, Version 2.0 Schrödinger, LLC) and Chimera[51] for visualization. The TM-scores were calculated respectively[47]. The AI-predicted model with the highest TM-score was used for further in silico experiments.

Protein structure preparation

Published crystal structures of hTRPC6 (PDB 5XY9) or hTRPC3 (PDB 5ZBG) and AI-predicted structures AF2-TRPC6, AF2-TRPC3, CF-TRPC6, CF-TRPC3, RT-TRPC6, RT-TRPC3 and EF-TRPC6 and EF-TRPC6 were loaded into Maestro (Schrödinger Release 2022-4: Maestro, Schrödinger, LLC, New York, NY, 2022)[50]. To prepare the protein for docking and simulations, the protein preparation wizard was used to assign bond orders, add hydrogens, create zero-order bonds to metals, create disulfide bonds, and fill in missing side chains and loops using Prime. Default parameters were used for the optimization of hydrogen-bond assignment.

Ligand structure preparation

Structures of **PPAP53** and hyperforin were drawn with ChemDraw, exported as SDF-files and imported to Maestro. LigPrep (Schrödinger Release 2022-3: LigPrep, Schrödinger, LLC, New York, NY, 2021.) was used to prepare **PPAP53** and hyperforin with default settings. Epik (Schrödinger Release 2022-3: Epik, Schrödinger, LLC, New York, NY, 2021.) was used to generating possible states at pH 7.0 ± 2.0 and retaining the specified stereochemical properties under physiological conditions applying the OPLS_2005 force field. Ligand preparation generated two possible ligand states for both compounds consisting of the corresponding (R)- and (S)- configured drug.

Molecular Docking

Receptor grids were generated for the generated binding site by selecting hyperforin as the grid-defining ligand for the hTRPC6, AF2-TRPC6, CF-TRPC6, TR-TRPC6, EF-TRPC6, hTRPC3, AF2-TRPC3, CF-TRPC3, TR-TRPC3 and EF-TRPC3 systems. The docking process was carried out using Glide (Schrödinger Release 2022-3: Glide, Schrödinger, LLC, New York, NY, 2021.) [52,53] with the default settings using standard precision (Glide SP module) and extra precision (Glide EXP module); no constraints were set. The obtained results were analyzed in terms of the scoring function values as well as the presence of binding interactions, favorable/unwilling contacts/clashes, and the repeatability of a given position. The best-ranked complex was selected for each compound.

Induced fit docking

The induced fit docking (IFD) program in the Schrödinger suite was also used in docking studies.[54] The program combines Glide docking with Prime conformational refinement. Initially, the ligands were docked using a softened potential with Glide SP. The Coulomb-vdW scaling factors were changed to 0.5 for both protein and ligand, and a maximum of 80 poses generated. The generated poses were further processed by Prime for side-chain refinements within 5 Å of the binding site, for better accommodation of the ligands. Thereafter, the systems were minimized with the OPLS_2005 force field.[55] In the final step, the ligands were redocked using Glide SP into the optimized protein structures generated within 30 kcal mol−1 of the lowest energy structure obtained after Prime refinement to generate 20 poses per system. The poses were ranked using the calculated IFD score (IFDScore = 1.0 × GlideScore + 0.05 × PrimeEnergy), and analyzed manually with the ligand interactions visualized and rendered using Maestro 13.4.129

(Schrödinger Release 2022-4: Maestro, Schrödinger, LLC, New York, NY, 2021.).[50]

ASSOCIATED CONTENT

Supporting Information

AUTHOR INFORMATION

Corresponding Author

Bernd Plietker – Technical University Dresden, Faculty of Chemistry and Food Chemistry, Department for Organic Chemistry I, Dresden 01069, Germany, Email: bernd.plietker@tu-dresden.de

Kristina Friedland - Pharm. & Tox. Institut für Biomedizinische und Pharmazeutische Wissenschaften Johannes Gutenberg-Universität Mainz, Mainz, Germany, Email: kfriedla@uni-mainz.de

Authors

Philipp Peslalz – Technical University Dresden, Faculty of Chemistry and Food Chemistry, Department for Organic Chemistry I, Dresden 01069, Germany; orcid.org/0000-0002-7427-5352.

Frank Kraus – Technical University Dresden, Faculty of Chemistry and Food Chemistry, Department for Organic Chemistry I, Dresden 01069, Germany.

Flavia Izzo – Technical University Dresden, Faculty of Chemistry and Food Chemistry, Department for Organic Chemistry I, Dresden 01069, Germany**;** orcid.org/0000-0002-4235-7070.

Anton Bleisch – Technical University Dresden, Faculty of Chemistry and Food Chemistry, Department for Organic Chemistry I, Dresden 01069, Germany.

Andreas Kany - Department of Pharmacy, Saarland University, 66123 Saarbrücken, Germany.; orcid.org/0000-0001-7580-3658.

Prof. Dr. Anna H. K. Hirsch - Department of Pharmacy, Saarland University, 66123 Saarbrücken, Germany; orcid.org/0000-0001-8734-4663.

Yamina El Hamdaoui - Pharm. & Tox. Institut für Biomedizinische und Pharmazeutische Wissenschaften Johannes Gutenberg-Universität Mainz, Mainz, Germany

Ina Schulz - Pharm. & Tox. Institut für Biomedizinische und Pharmazeutische Wissenschaften Johannes Gutenberg-Universität Mainz, Mainz, Germany

Author Contributions

‡These authors contributed equally.

Funding Sources

Financial support by the Ministerium für Wissenschaft und Kultur Baden-Württemberg is gratefully acknowledged.

ACKNOWLEDGMENT

We thank Selina Wolter and Philipp Gansen for their technical assistance.

REFERENCES

(1) Lee, A.; Fakler, B.; Kaczmarek, L. K.; Isom, L. L. More Than a Pore: Ion Channel Signaling Complexes. *J Neurosci* **2014**, *34* (46), 15159–15169. https://doi.org/10.1523/JNEUROSCI.3275-14.2014.

(2) Hellmich, U. A.; Gaudet, R. Structural Biology of TRP Channels. In *Mammalian Transient Receptor Potential (TRP) Cation Channels: Volume II*; Nilius, B., Flockerzi, V., Eds.; Handbook of Experimental Pharmacology; Springer International Publishing: Cham, 2014; pp 963–990. https://doi.org/10.1007/978-3-319-05161-1_10.

(3) Himmel, N. J.; Cox, D. N. Transient Receptor Potential Channels: Current Perspectives on Evolution, Structure, Function and Nomenclature. *Proceedings of the Royal Society B: Biological Sciences* **2020**, *287* (1933), 20201309. https://doi.org/10.1098/rspb.2020.1309.

(4) Wang, H.; Cheng, X.; Tian, J.; Xiao, Y.; Tian, T.; Xu, F.; Hong, X.; Zhu, M. X. TRPC Channels: Structure, Function, Regulation and Recent Advances in Small Molecular Probes. *Pharmacology & Therapeutics* **2020**, *209*, 107497. https://doi.org/10.1016/j.pharmthera.2020.107497.

(5) Bacsa, B.; Tiapko, O.; Stockner, T.; Groschner, K. Mechanisms and Significance of Ca2+ Entry through TRPC Channels. *Current Opinion in Physiology* **2020**, *17*, 25–33. https://doi.org/10.1016/j.cophys.2020.06.005.

(6) Nagy, G. A.; Botond, G.; Borhegyi, Z.; Plummer, N. W.; Freund, T. F.; Hájos, N. DAG-Sensitive and Ca(2+) Permeable TRPC6 Channels Are Expressed in Dentate Granule Cells and Interneurons in the Hippocampal Formation. *Hippocampus* **2013**, *23* (3), 221–232. https://doi.org/10.1002/hipo.22081.

(7) Leuner, K.; Li, W.; Amaral, M. D.; Rudolph, S.; Calfa, G.; Schuwald, A. M.; Harteneck, C.; Inoue, T.; Pozzo-Miller, L. Hyperforin Modulates Dendritic Spine Morphology in Hippocampal Pyramidal Neurons by Activating Ca2+-Permeable TRPC6 Channels. *Hippocampus* **2013**, *23* (1), 40–52. https://doi.org/10.1002/hipo.22052.

(8) Li, Y.; Jia, Y.-C.; Cui, K.; Li, N.; Zheng, Z.-Y.; Wang, Y.; Yuan, X. Essential Role of TRPC Channels in the Guidance of Nerve Growth Cones by Brain-Derived Neurotrophic Factor. *Nature* **2005**, *434* (7035), 894–898. https://doi.org/10.1038/nature03477.

(9) Zhou, J.; Du, W.; Zhou, K.; Tai, Y.; Yao, H.; Jia, Y.; Ding, Y.; Wang, Y. Critical Role of TRPC6 Channels in the Formation of Excitatory Synapses. *Nat Neurosci* **2008**, *11* (7), 741–743. https://doi.org/10.1038/nn.2127.

(10) Li, J.; Zhang, X.; Song, X.; Liu, R.; Zhang, J.; Li, Z. The Structure of TRPC Ion Channels. *Cell Calcium* **2019**, *80*, 25–28. https://doi.org/10.1016/j.ceca.2019.03.005.

(11) Bai, Y.; Yu, X.; Chen, H.; Horne, D.; White, R.; Wu, X.; Lee, P.; Gu, Y.; Ghimire-Rijal, S.; Lin, D. C.-H.; Huang, X. Structural Basis for Pharmacological Modulation of the TRPC6 Channel. *eLife* **2020**, *9*, e53311. https://doi.org/10.7554/eLife.53311.

(12) Azumaya, C. M.; Sierra-Valdez, F.; Cordero-Morales, J. F.; Nakagawa, T. Cryo-EM Structure of the Cytoplasmic Domain of Murine Transient Receptor Potential Cation Channel Subfamily C Member 6 (TRPC6). *Journal of Biological Chemistry* **2018**, *293* (26), 10381–10391. https://doi.org/10.1074/jbc.RA118.003183.

(13) Yang, P.-L.; Li, X.-H.; Wang, J.; Ma, X.-F.; Zhou, B.-Y.; Jiao, Y.-F.; Wang, W.-H.; Cao, P.; Zhu, M. X.; Li, P.-W.; Xiao, Z.-H.; Li, C.-Z.; Guo, C.-R.; Lei, Y.-T.; Yu, Y. GSK1702934A and M085 Directly Activate TRPC6 via a Mechanism of Stimulating the Extracellular Cavity Formed by the Pore Helix and Transmembrane Helix S6. *Journal of Biological*

Chemistry **2021**, *297* (4), 101125. https://doi.org/10.1016/j.jbc.2021.101125.

(14) Linde, K.; Ramirez, G.; Mulrow, C. D.; Pauls, A.; Weidenhammer, W.; Melchart, D. St John's Wort for Depression—an Overview and Meta-Analysis of Randomised Clinical Trials. *BMJ* **1996**, *313* (7052), 253–258. https://doi.org/10.1136/bmj.313.7052.253.

(15) Linde, K.; Berner, M. M.; Kriston, L. St John's Wort for Major Depression. *Cochrane Database of Systematic Reviews* **2008**, No. 4. https://doi.org/10.1002/14651858.CD000448.pub3.

(16) Apaydin, E. A.; Maher, A. R.; Shanman, R.; Booth, M. S.; Miles, J. N. V.; Sorbero, M. E.; Hempel, S. A Systematic Review of St. John's Wort for Major Depressive Disorder. *Systematic Reviews* **2016**, *5* (1), 148. https://doi.org/10.1186/s13643-016-0325-2.

(17) Leuner, K.; Kazanski, V.; Muller, M.; Essin, K.; Henke, B.; Gollasch, M.; Harteneck, C.; Müller, W. E. Hyperforin—a Key Constituent of St. John's Wort Specifically Activates TRPC6 Channels. *The FASEB Journal* **2007**, *21* (14), 4101–4111. https://doi.org/10.1096/fj.07-8110com.

(18) Kandel, B. A.; Ekins, S.; Leuner, K.; Thasler, W. E.; Harteneck, C.; Zanger, U. M. No Activation of Human Pregnane X Receptor by Hyperforin-Related Phloroglucinols. *J Pharmacol Exp Ther* **2014**, *348* (3), 393–400. https://doi.org/10.1124/jpet.113.209916.

(19) Cossuta, D.; Vatai, T.; Báthori, M.; Hohmann, J.; Keve, T.; Simándi, B. Extraction of Hyperforin and Hypericin from St. John's Wort (Hypericum Perforatum L.) with Different Solvents. *Journal of Food Process Engineering* **2012**, *35* (2), 222–235. https://doi.org/10.1111/j.1745-4530.2010.00583.x.

(20) Komoroski, B. J.; Zhang, S.; Cai, H.; Hutzler, J. M.; Frye, R.; Tracy, T. S.; Strom, S. C.; Lehmann, T.; Ang, C. Y. W.; Cui, Y. Y.; Venkataramanan, R. Induction and Inhibition of Cytochromes P450 by the St. John's Wort Constituent Hyperforin in Human Hepatocyte Cultures. *Drug Metab Dispos* **2004**, *32* (5), 512–518. https://doi.org/10.1124/dmd.32.5.512.

(21) El Hamdaoui, Y.; Zheng, F.; Fritz, N.; Ye, L.; Tran, M. A.; Schwickert, K.; Schirmeister, T.; Braeuning, A.; Lichtenstein, D.; Hellmich, U. A.; Weikert, D.; Heinrich, M.; Treccani, G.; Schäfer, M. K. E.; Nowak, G.; Nürnberg, B.; Alzheimer, C.; Müller, C. P.; Friedland, K. Analysis of Hyperforin (St. John's Wort) Action at TRPC6 Channel Leads to the Development of a New Class of Antidepressant Drugs. *Mol Psychiatry* **2022**, 1–16. https://doi.org/10.1038/s41380-022-01804-3.

(22) Yang, X.-W.; Grossman, R. B.; Xu, G. Research Progress of Polycyclic Polyprenylated Acylphloroglucinols. *Chem. Rev.* **2018**, *118* (7), 3508–3558. https://doi.org/10.1021/acs.chemrev.7b00551.

(23) Ciochina, R.; Grossman, R. B. Polycyclic Polyprenylated Acylphloroglucinols. *Chem. Rev.* **2006**, *106* (9), 3963–3986. https://doi.org/10.1021/cr0500582.

(24) Abramova, I.; Rudshteyn, B.; Liebman, J. F.; Greer, A. Computed Regioselectivity and Conjectured Biological Activity of Ene Reactions of Singlet Oxygen with the Natural Product Hyperforin. *Photochemistry and Photobiology* **2017**, *93* (2), 626–631. https://doi.org/10.1111/php.12706.

(25) Meinke, M. C.; Schanzer, S.; Haag, S. F.; Casetti, F.; Müller, M. L.; Wölfle, U.; Kleemann, A.; Lademann, J.; Schempp, C. M. In Vivo Photoprotective and Anti-Inflammatory Effect of Hyperforin Is Associated with High Antioxidant Activity in Vitro and Ex Vivo. *European Journal of Pharmaceutics and Biopharmaceutics* **2012**, *81* (2), 346–350. https://doi.org/10.1016/j.ejpb.2012.03.002.

(26) Guttroff, C.; Baykal, A.; Wang, H.; Popella, P.; Kraus, F.; Biber, N.; Krauss, S.; Götz, F.; Plietker, B. Polycyclic Polyprenylated Acylphloroglucinols: An Emerging Class of Non-Peptide-Based MRSA- and VRE-Active Antibiotics. *Angewandte Chemie International Edition* **2017**, *56* (50), 15852–15856. https://doi.org/10.1002/anie.201707069.

(27) Biber, N.; Möws, K.; Plietker, B. The Total Synthesis of Hyperpapuanone, Hyperibone L, Epi-Clusianone and Oblongifolin A. *Nature Chem* **2011**, *3* (12), 938–942. https://doi.org/10.1038/nchem.1170.

(28) Lindermayr, K.; Plietker, B. The Bidirectional Total Synthesis of Sampsonione P and Hyperibone I. *Angewandte Chemie International Edition* **2013**, *52* (46), 12183–12186. https://doi.org/10.1002/anie.201306256.

(29) Horeischi, F.; Biber, N.; Plietker, B. The Total Syntheses of Guttiferone A and 6-Epi-Guttiferone A. *J. Am. Chem. Soc.* **2014**, *136* (10), 4026–4030. https://doi.org/10.1021/ja500063a.

(30) Horeischi, F.; Guttroff, C.; Plietker, B. The Enantioselective Total Synthesis of (+)-Clusianone. *Chem. Commun.* **2015**, *51* (12), 2259–2261. https://doi.org/10.1039/C4CC09701G.

(31) Socolsky, C.; Plietker, B. Total Synthesis and Absolute Configuration Assignment of MRSA Active Garcinol and Isogarcinol. *Chemistry – A European Journal* **2015**, *21* (7), 3053–3061. https://doi.org/10.1002/chem.201406077.

(32) Schempp, C. M.; Pelz, K.; Wittmer, A.; Schöpf, E.; Simon, J. C. Antibacterial Activity of Hyperforin from St John's Wort, against Multiresistant Staphylococcus Aureus and Gram-Positive Bacteria. *Lancet* **1999**, *353* (9170), 2129. https://doi.org/10.1016/S0140-6736(99)00214-7.

(33) Leuner, K.; Kraus, M.; Woelfle, U.; Beschmann, H.; Harteneck, C.; Boehncke, W.-H.; Schempp, C. M.; Müller, W. E. Reduced TRPC Channel Expression in Psoriatic Keratinocytes Is Associated with Impaired Differentiation and Enhanced Proliferation. *PLOS ONE* **2011**, *6* (2), e14716. https://doi.org/10.1371/journal.pone.0014716.

(34) Heiser, J. H.; Schuwald, A. M.; Sillani, G.; Ye, L.; Müller, W. E.; Leuner, K. TRPC6 Channel-Mediated Neurite Outgrowth in PC12 Cells and Hippocampal Neurons Involves Activation of RAS/MEK/ERK, PI3K, and CAMKIV Signaling. *J Neurochem* **2013**, *127* (3), 303–313. https://doi.org/10.1111/jnc.12376.

(35) Fan, C.; Choi, W.; Sun, W.; Du, J.; Lü, W. Structure of the Human Lipid-Gated Cation Channel TRPC3. *eLife* **2018**, *7*, e36852. https://doi.org/10.7554/eLife.36852.

(36) Tang, Q.; Guo, W.; Zheng, L.; Wu, J.-X.; Liu, M.; Zhou, X.; Zhang, X.; Chen, L. Structure of the Receptor-Activated Human TRPC6 and TRPC3 Ion Channels. *Cell Res* **2018**, *28* (7), 746–755. https://doi.org/10.1038/s41422-018-0038-2.

(37) Jumper, J.; Evans, R.; Pritzel, A.; Green, T.; Figurnov, M.; Ronneberger, O.; Tunyasuvunakool, K.; Bates, R.; Žídek, A.; Potapenko, A.; Bridgland, A.; Meyer, C.; Kohl, S. A. A.; Ballard, A. J.; Cowie, A.; Romera-Paredes, B.; Nikolov, S.; Jain, R.; Adler, J.; Back, T.; Petersen, S.; Reiman, D.; Clancy, E.; Zielinski, M.; Steinegger, M.; Pacholska, M.; Berghammer, T.; Bodenstein, S.; Silver, D.; Vinyals, O.; Senior, A.

W.; Kavukcuoglu, K.; Kohli, P.; Hassabis, D. Highly Accurate Protein Structure Prediction with AlphaFold. *Nature* **2021**, *596* (7873), 583–589. https://doi.org/10.1038/s41586-021-03819-2.

(38) Baek, M.; DiMaio, F.; Anishchenko, I.; Dauparas, J.; Ovchinnikov, S.; Lee, G. R.; Wang, J.; Cong, Q.; Kinch, L. N.; Schaeffer, R. D.; Millán, C.; Park, H.; Adams, C.; Glassman, C. R.; DeGiovanni, A.; Pereira, J. H.; Rodrigues, A. V.; van Dijk, A. A.; Ebrecht, A. C.; Opperman, D. J.; Sagmeister, T.; Buhlheller, C.; Pavkov-Keller, T.; Rathinaswamy, M. K.; Dalwadi, U.; Yip, C. K.; Burke, J. E.; Garcia, K. C.; Grishin, N. V.; Adams, P. D.; Read, R. J.; Baker, D. Accurate Prediction of Protein Structures and Interactions Using a Three-Track Neural Network. *Science* **2021**, *373* (6557), 871–876. https://doi.org/10.1126/science.abj8754.

(39) Wu, R.; Ding, F.; Wang, R.; Shen, R.; Zhang, X.; Luo, S.; Su, C.; Wu, Z.; Xie, Q.; Berger, B.; Ma, J.; Peng, J. High-Resolution de Novo Structure Prediction from Primary Sequence. bioRxiv July 22, 2022, p 2022.07.21.500999. https://doi.org/10.1101/2022.07.21.500999.

(40) Lin, Z.; Akin, H.; Rao, R.; Hie, B.; Zhu, Z.; Lu, W.; Costa, A. dos S.; Fazel-Zarandi, M.; Sercu, T.; Candido, S.; Rives, A. Language Models of Protein Sequences at the Scale of Evolution Enable Accurate Structure Prediction. bioRxiv July 21, 2022, p 2022.07.20.500902. https://doi.org/10.1101/2022.07.20.500902.

(41) Chowdhury, R.; Bouatta, N.; Biswas, S.; Rochereau, C.; Church, G. M.; Sorger, P. K.; AlQuraishi, M. Single-Sequence Protein Structure Prediction Using Language Models from Deep Learning. bioRxiv August 4, 2021, p 2021.08.02.454840. https://doi.org/10.1101/2021.08.02.454840.

(42) Greener, J. G.; Kandathil, S. M.; Jones, D. T. Deep Learning Extends de Novo Protein Modelling Coverage of Genomes Using Iteratively Predicted Structural Constraints. *Nat Commun* **2019**, *10* (1), 3977. https://doi.org/10.1038/s41467-019-11994-0.

(43) Hopf, T. A.; Green, A. G.; Schubert, B.; Mersmann, S.; Schärfe, C. P. I.; Ingraham, J. B.; Toth-Petroczy, A.; Brock, K.; Riesselman, A. J.; Palmedo, P.; Kang, C.; Sheridan, R.; Draizen, E. J.; Dallago, C.; Sander, C.; Marks, D. S. The EVcouplings Python Framework for Coevolutionary Sequence Analysis. *Bioinformatics* **2019**, *35* (9), 1582–1584. https://doi.org/10.1093/bioinformatics/bty862.

(44) Hegedűs, T.; Geisler, M.; Lukács, G. L.; Farkas, B. Ins and Outs of AlphaFold2 Transmembrane Protein Structure Predictions. *Cell. Mol. Life Sci.* **2022**, *79* (1), 73. https://doi.org/10.1007/s00018-021-04112-1.

(45) Mirdita, M.; Schütze, K.; Moriwaki, Y.; Heo, L.; Ovchinnikov, S.; Steinegger, M. ColabFold: Making Protein Folding Accessible to All. *Nat Methods* **2022**, *19* (6), 679–682. https://doi.org/10.1038/s41592-022-01488-1.

(46) Du, Z.; Su, H.; Wang, W.; Ye, L.; Wei, H.; Peng, Z.; Anishchenko, I.; Baker, D.; Yang, J. The TrRosetta Server for Fast and Accurate Protein Structure Prediction. *Nat Protoc* **2021**, *16* (12), 5634–5651. https://doi.org/10.1038/s41596-021-00628-9.

(47) Zhang, Y.; Skolnick, J. Scoring Function for Automated Assessment of Protein Structure Template Quality. *Proteins* **2004**, *57* (4), 702–710. https://doi.org/10.1002/prot.20264.

(48) Ang, C. Y. W.; Hu, L.; Heinze, T. M.; Cui, Y.; Freeman, J. P.; Kozak, K.; Luo, W.; Liu, F. F.; Mattia, A.; DiNovi, M. Instability of St. John's Wort (Hypericum Perforatum L.) and Degradation of Hyperforin in Aqueous Solutions and Functional Beverage. *J Agric Food Chem* **2004**, *52* (20), 6156–6164. https://doi.org/10.1021/jf0490596.

(49) Varadi, M.; Anyango, S.; Deshpande, M.; Nair, S.; Natassia, C.; Yordanova, G.; Yuan, D.; Stroe, O.; Wood, G.; Laydon, A.; Žídek, A.; Green, T.; Tunyasuvunakool, K.; Petersen, S.; Jumper, J.; Clancy, E.; Green, R.; Vora, A.; Lutfi, M.; Figurnov, M.; Cowie, A.; Hobbs, N.; Kohli, P.; Kleywegt, G.; Birney, E.; Hassabis, D.; Velankar, S. AlphaFold Protein Structure Database: Massively Expanding the Structural Coverage of Protein-Sequence Space with High-Accuracy Models. *Nucleic Acids Research* **2022**, *50* (D1), D439–D444. https://doi.org/10.1093/nar/gkab1061.

(50) Schrödinger Release 2023-1: Maestro, Schrödinger, LLC, New York, NY, 2021..

(51) Pettersen, E. F.; Goddard, T. D.; Huang, C. C.; Couch, G. S.; Greenblatt, D. M.; Meng, E. C.; Ferrin, T. E. UCSF Chimera—A Visualization System for Exploratory Research and Analysis. *Journal of Computational Chemistry* **2004**, *25* (13), 1605–1612. https://doi.org/10.1002/jcc.20084.

(52) Friesner, R. A.; Banks, J. L.; Murphy, R. B.; Halgren, T. A.; Klicic, J. J.; Mainz, D. T.; Repasky, M. P.; Knoll, E. H.; Shelley, M.; Perry, J. K.; Shaw, D. E.; Francis, P.; Shenkin, P. S. Glide: A New Approach for Rapid, Accurate Docking and Scoring. 1. Method and Assessment of Docking Accuracy. *J. Med. Chem.* **2004**, *47* (7), 1739–1749. https://doi.org/10.1021/jm0306430.

(53) Halgren, T. A.; Murphy, R. B.; Friesner, R. A.; Beard, H. S.; Frye, L. L.; Pollard, W. T.; Banks, J. L. Glide: A New Approach for Rapid, Accurate Docking and Scoring. 2. Enrichment Factors in Database Screening. *J. Med. Chem.* **2004**, *47* (7), 1750–1759. https://doi.org/10.1021/jm030644s.

(54) Sherman, W.; Beard, H. S.; Farid, R. Use of an Induced Fit Receptor Structure in Virtual Screening. *Chemical Biology & Drug Design* **2006**, *67* (1), 83–84. https://doi.org/10.1111/j.1747-0285.2005.00327.x.

(55) Banks, J. L.; Beard, H. S.; Cao, Y.; Cho, A. E.; Damm, W.; Farid, R.; Felts, A. K.; Halgren, T. A.; Mainz, D. T.; Maple, J. R.; Murphy, R.; Philipp, D. M.; Repasky, M. P.; Zhang, L. Y.; Berne, B. J.; Friesner, R. A.; Gallicchio, E.; Levy, R. M. Integrated Modeling Program, Applied Chemical Theory (IMPACT). *J Comput Chem* **2005**, *26* (16), 1752–1780. https://doi.org/10.1002/jcc.20292.

Supporting Information

Selective Activation of TRPC6 Ion Channel by Metallated Type-B Polyprenylated Polycyclic Acylphloroglucinols

Philipp Peslalz[‡1], Frank Kraus[‡1], Flavia Izzo[1], Anton Bleisch[1], Yamina El Hamdaoui[2], Ina Schulz[2], Andreas M. Kany[3], Anna K. H. Hirsch[3,4], Kristina Friedland*[2], Bernd Plietker*[1]

[1] Chair of Organic Chemistry, Faculty of Chemistry and Food Chemistry, Technical University Dresden, Bergstr. 66, 01069 Dresden, Germany.

[2] Pharm. & Tox. Institut für Biomedizinische und Pharmazeutische Wissenschaften Johannes Gutenberg-Universität Mainz, Mainz, Germany.

[3] Helmholtz Institute for Pharm. Research Saarland, (HIPS)–Helmholtz Centre for Infection Research (HZI); Saarbrücken, 66123, Germany.

[4] Department of Pharmacy, Saarland University, 66123 Saarbrücken, Germany.

Corresponding Authors

Prof. Dr. Bernd Plietker bernd.plietker@tu-dresden.de

Prof. Dr. Kristina Friedland kfriedla@uni-mainz.de

Table of contents

1. Predicted TRPC models

1.1 CF-TRPC6 models

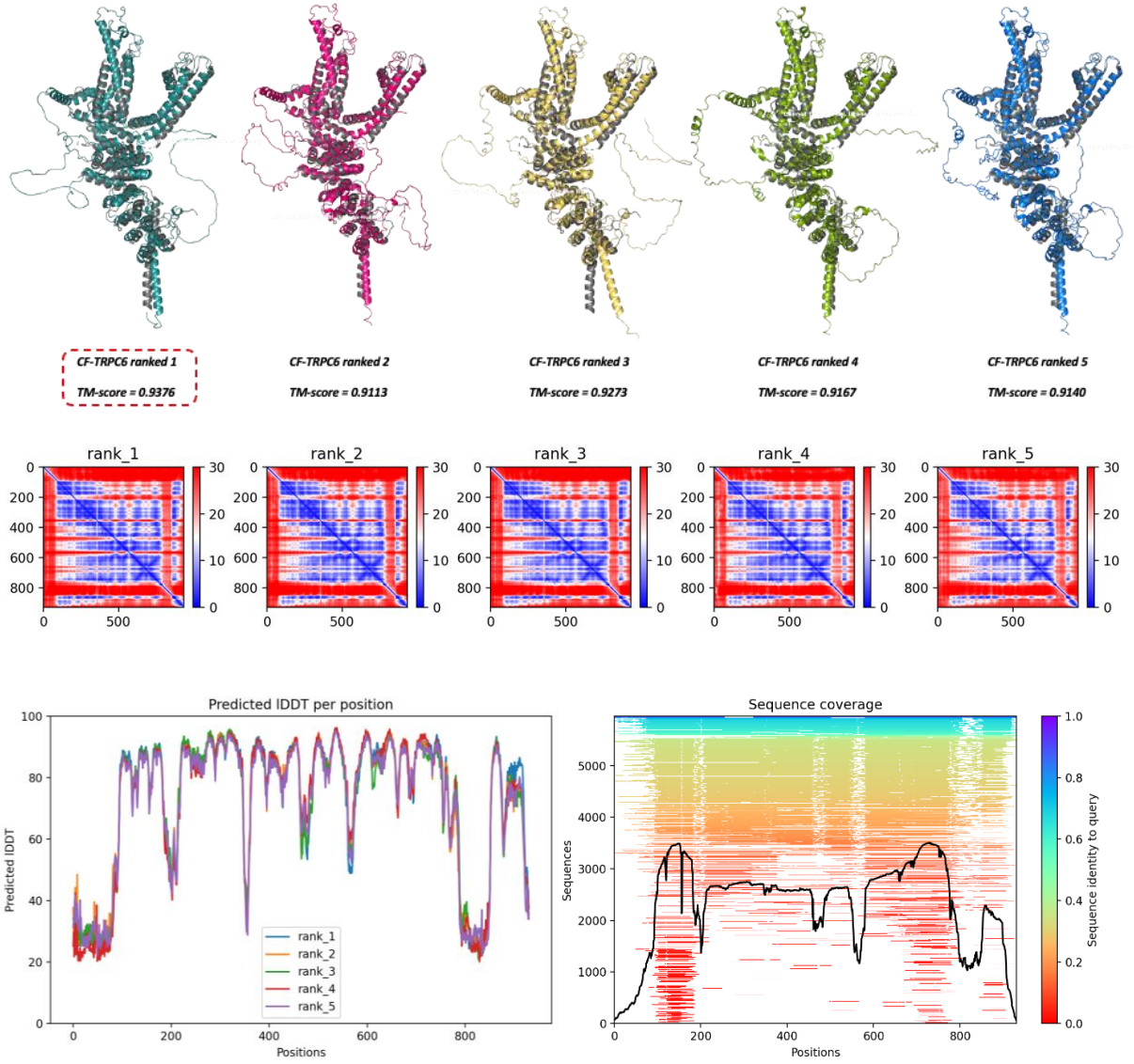

SI Figure 1 TRPC6 models predicted with ColabFold under default conditions and ranked by model confidence. The predicted models (teal, red, yellow, green and blue) are shown as overlays with the crystal structure (grey) (PDB-ID 5XY9) with corresponding Predicted Aligned Error (PAE), plDDT values und sequence coverage.

1.2 CF-TRPC3 monomer models

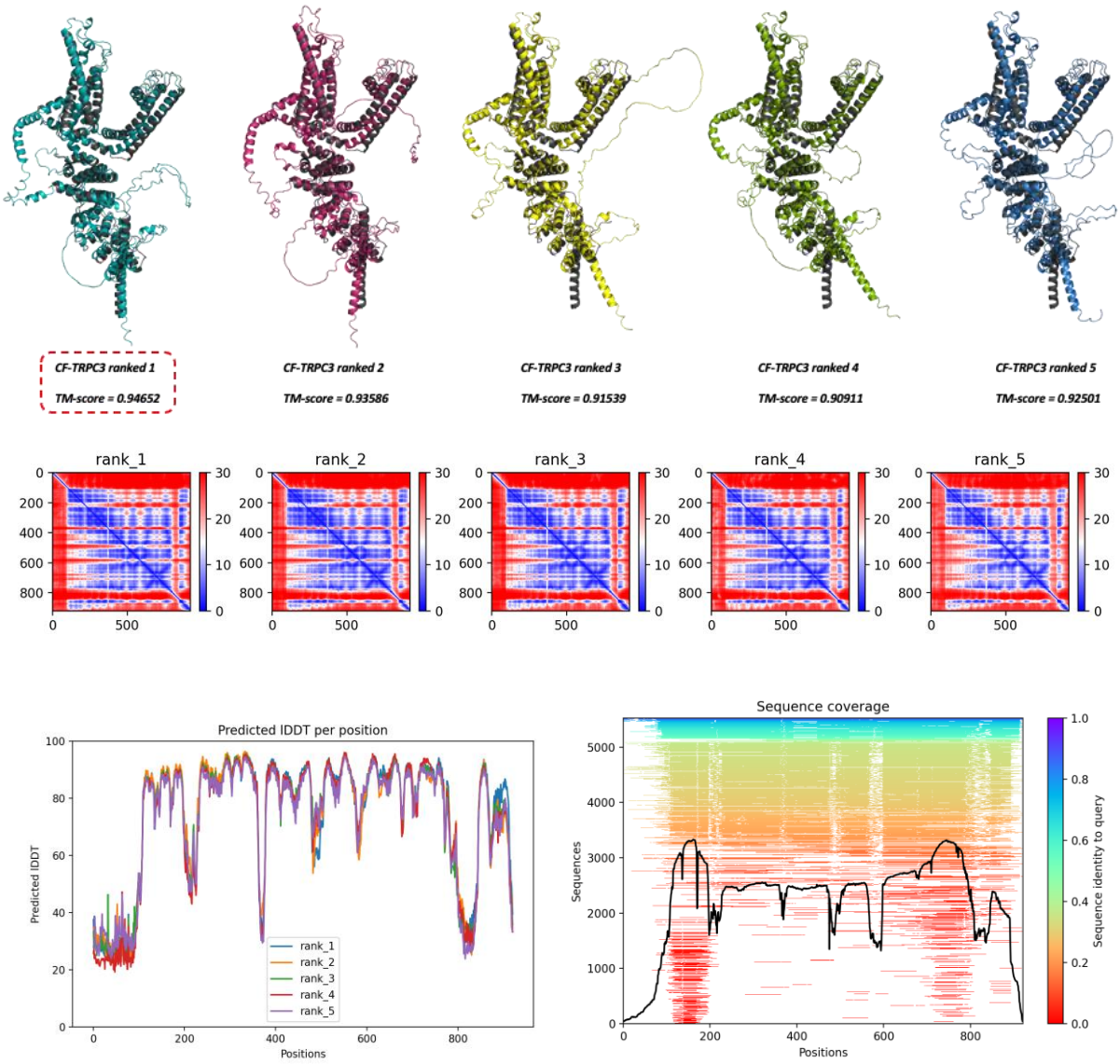

SI Figure 2 TRPC3 models predicted with ColabFold under default conditions and ranked by model confidence. The predicted models (teal, red, yellow, green and blue) are shown as overlays with the crystal structure (grey) (PDB-ID 5XY9) with corresponding Predicted Aligned Error (PAE), plDDT values und sequence coverage.

1.3 RT-TRPC6-monomer models

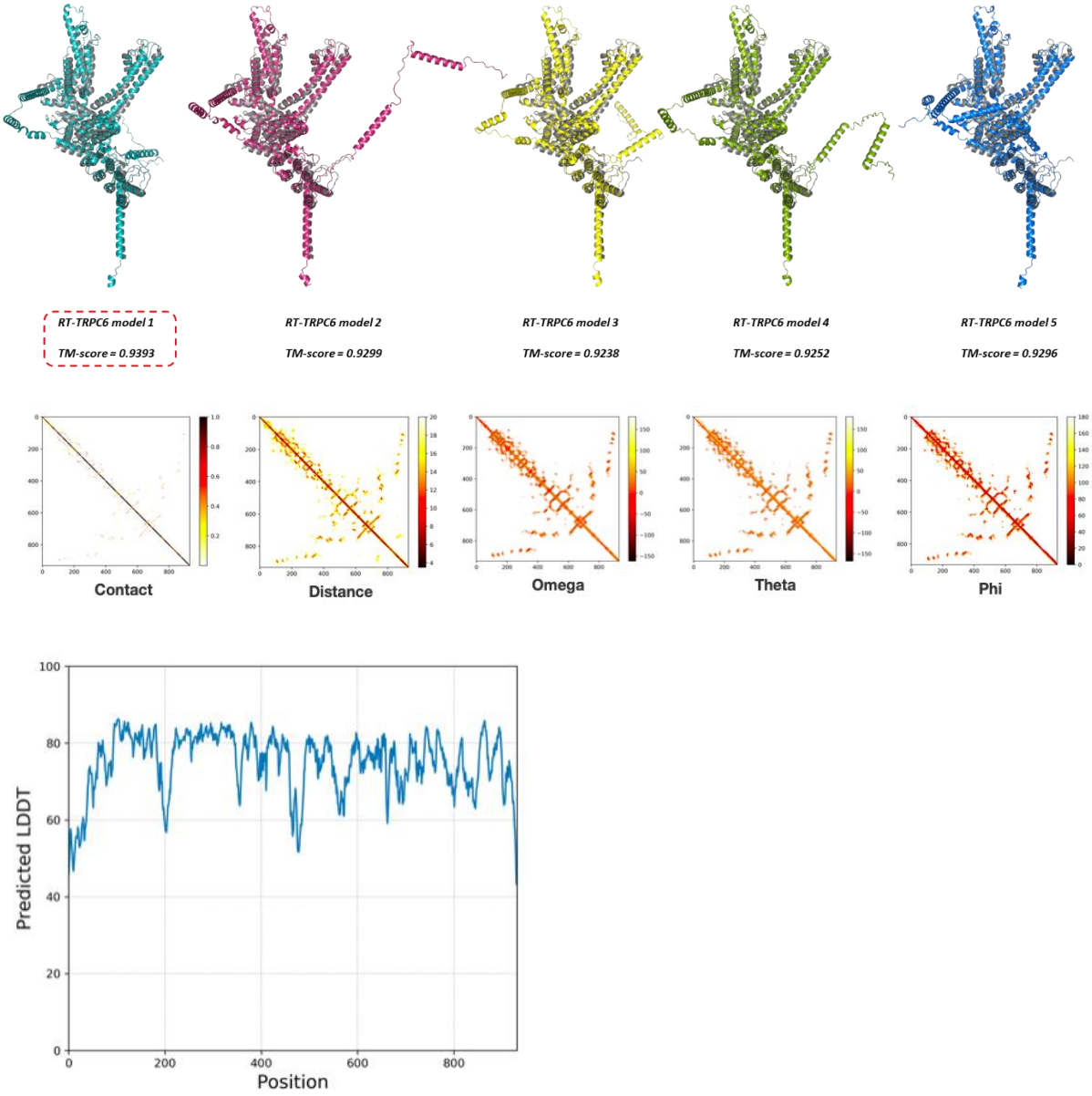

SI Figure 3 TRPC6 models predicted with trRosetta under default conditions and ranked by model confidence. The predicted models (teal, red, yellow, green and blue) are shown as overlays with the crystal structure (grey) (PDB-ID 5XY9) with corresponding Predicted Aligned Error (PAE), plDDT values und sequence coverage.

1.4 RT-TRPC3-monomer models

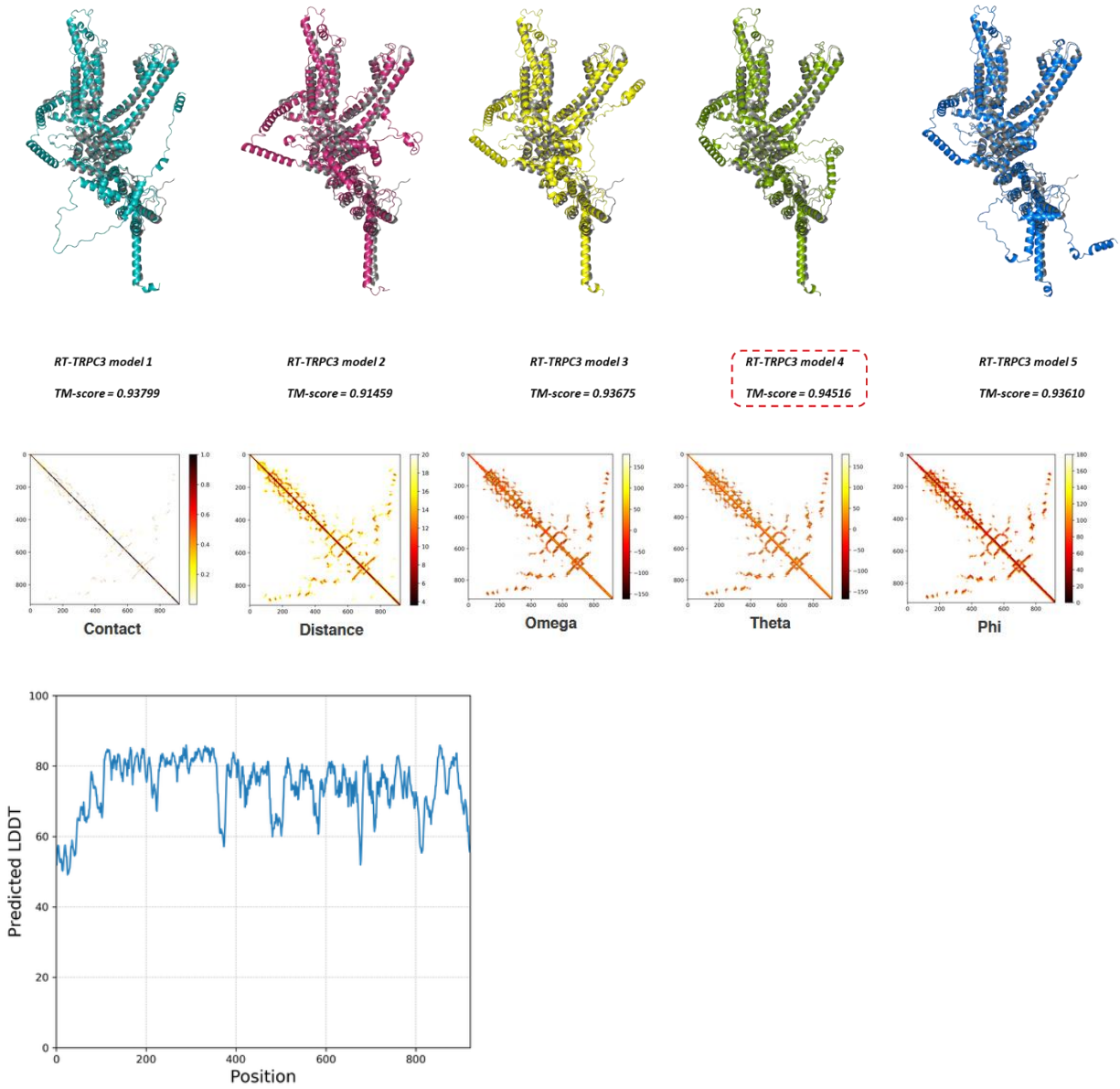

SI Figure 4 TRPC3 models predicted with trRosetta under default conditions and ranked by model confidence. The predicted models (teal, red, yellow, green and blue) are shown as overlays with the crystal structure (grey) (PDB-ID 5XY9) with corresponding Predicted Aligned Error (PAE), plDDT values und sequence coverage.

1.5 EF-TRPC6-monomer model

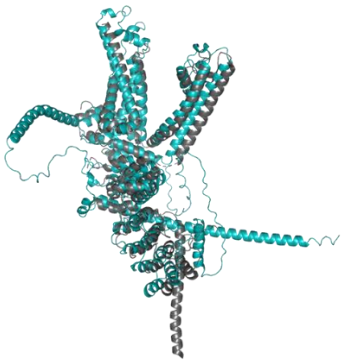

EF-TRPC6 model 1

TM-score = 0,8134

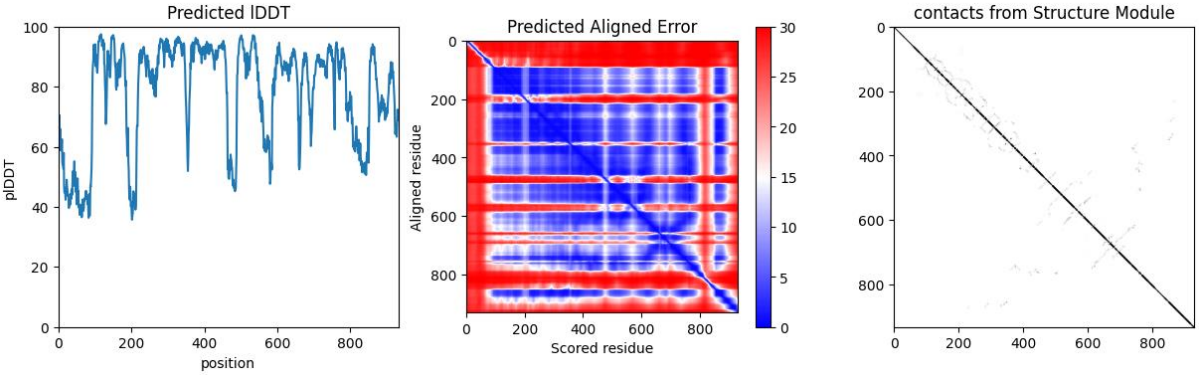

SI Figure 5 TRPC6 model predicted with ESM-Fold under default conditions and ranked by model confidence. The predicted model (teal) is shown as overlay with the crystal structure (grey) (PDB-ID 5XY9) with corresponding Predicted Aligned Error (PAE), plDDT values und contacts from structure modules

1.6 EF-TRPC3-monomer model

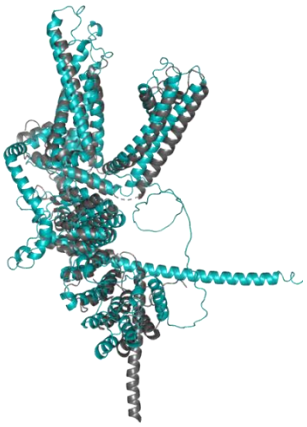

EF-TRPC3 model 1

TM-score = 0,81719

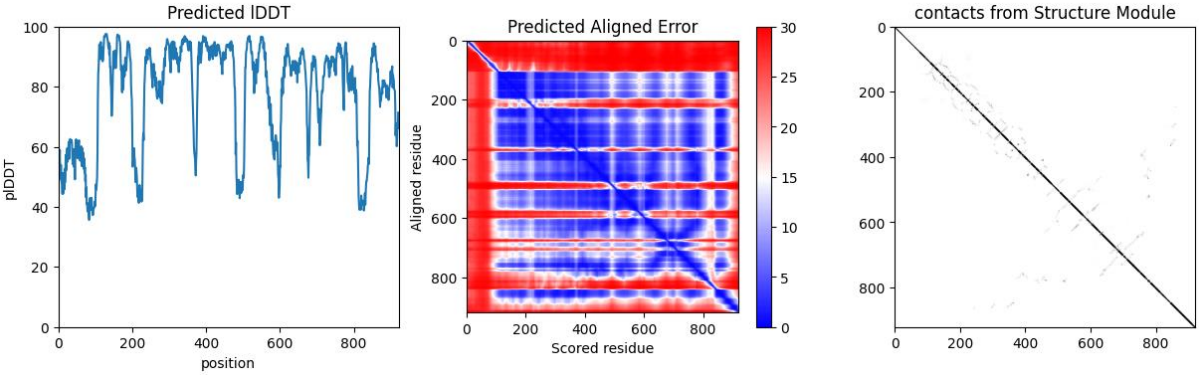

SI Figure 6 TRPC3 model predicted with ESM-Fold under default conditions and ranked by model confidence. The predicted model (teal) is shown as overlay with the crystal structure (grey) (PDB-ID 5XY9) with corresponding Predicted Aligned Error (PAE), plDDT values und contacts from structure modules

2. Molecular Docking

2.1 Binding mode of PPAP 53 in CF-TRPC6

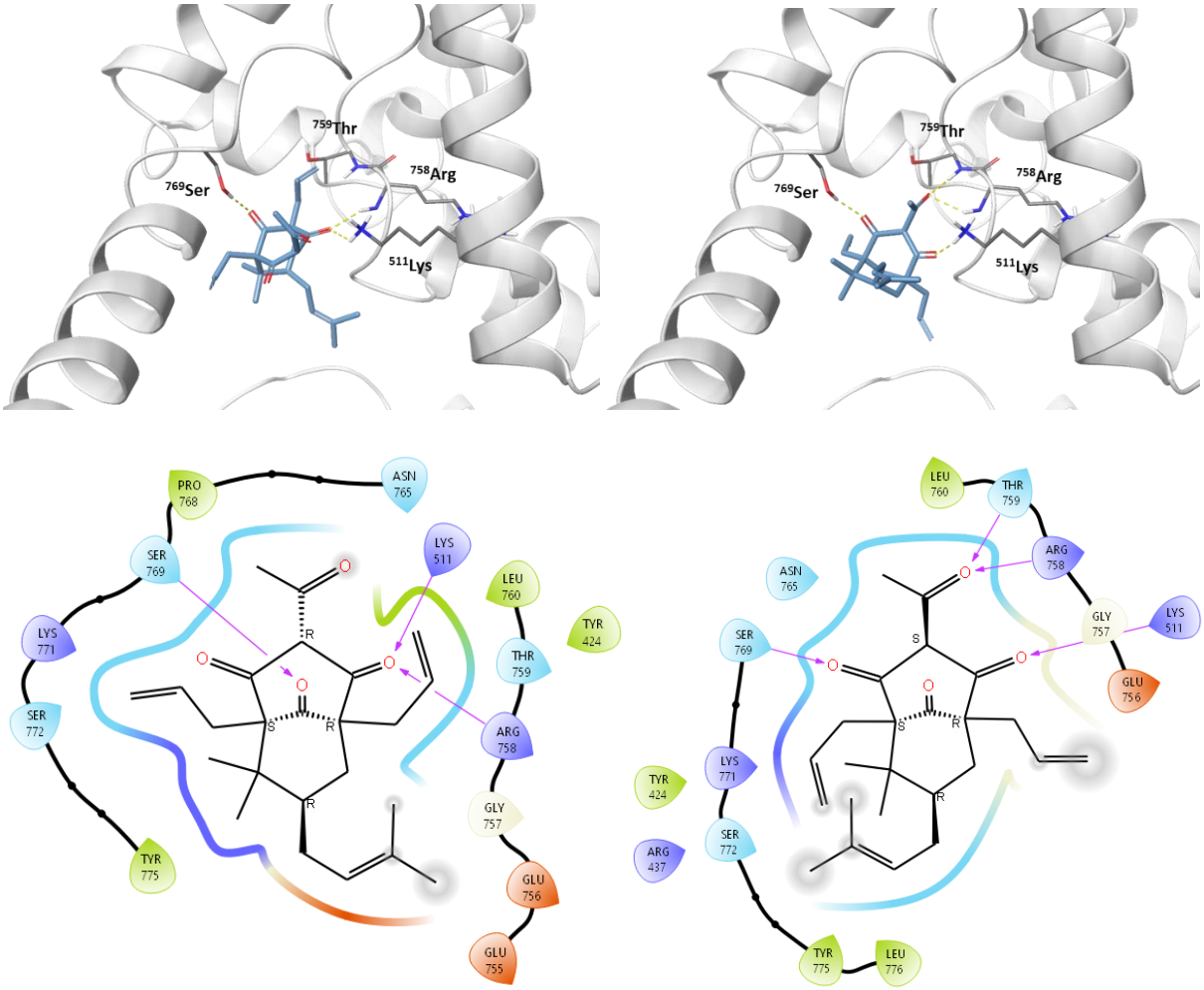

SI Figure 7 Binding mode of both PPAP53 isomers (blue) within CF-TRPC6 (white) with corresponding 2D ligand interaction diagram. The violet lines indicate hydrogen bond interactions. The polar and hydrophobic residues are highlighted in blue and green, positive and negative charged residues are highlighted in purple and red respectively.

2.2 Binding mode of Hyperforin in CF-TRPC6

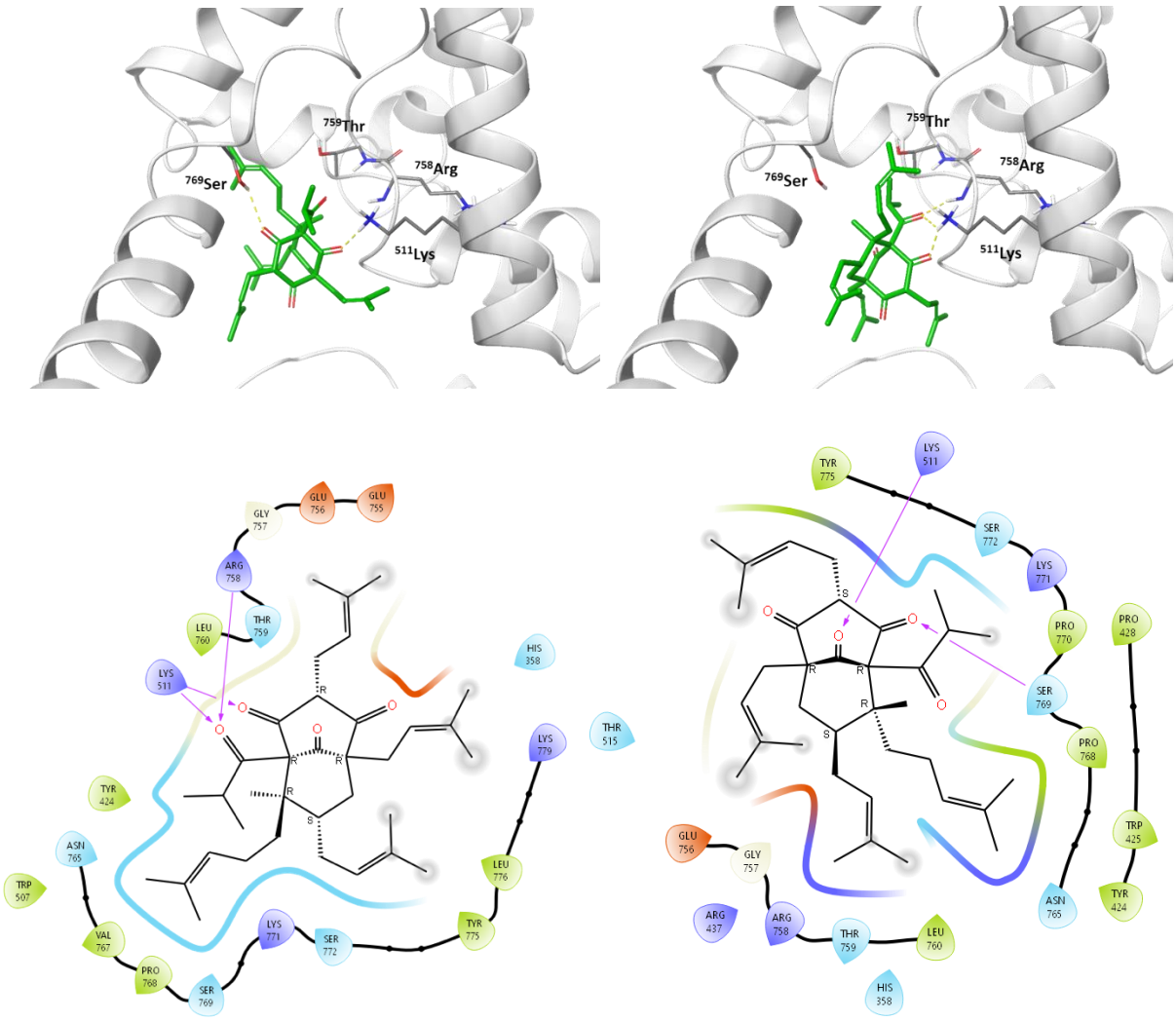

SI Figure 8 Binding mode of both hyperforin isomers (green) within CF-TRPC6 (white) with corresponding 2D ligand interaction diagram. The violet lines indicate hydrogen bond interactions. The polar and hydrophobic residues are highlighted in blue and green, positive and negative charged residues are highlighted in purple and red respectively.

2.3 Binding mode of PPAP53 in RT-TRPC6

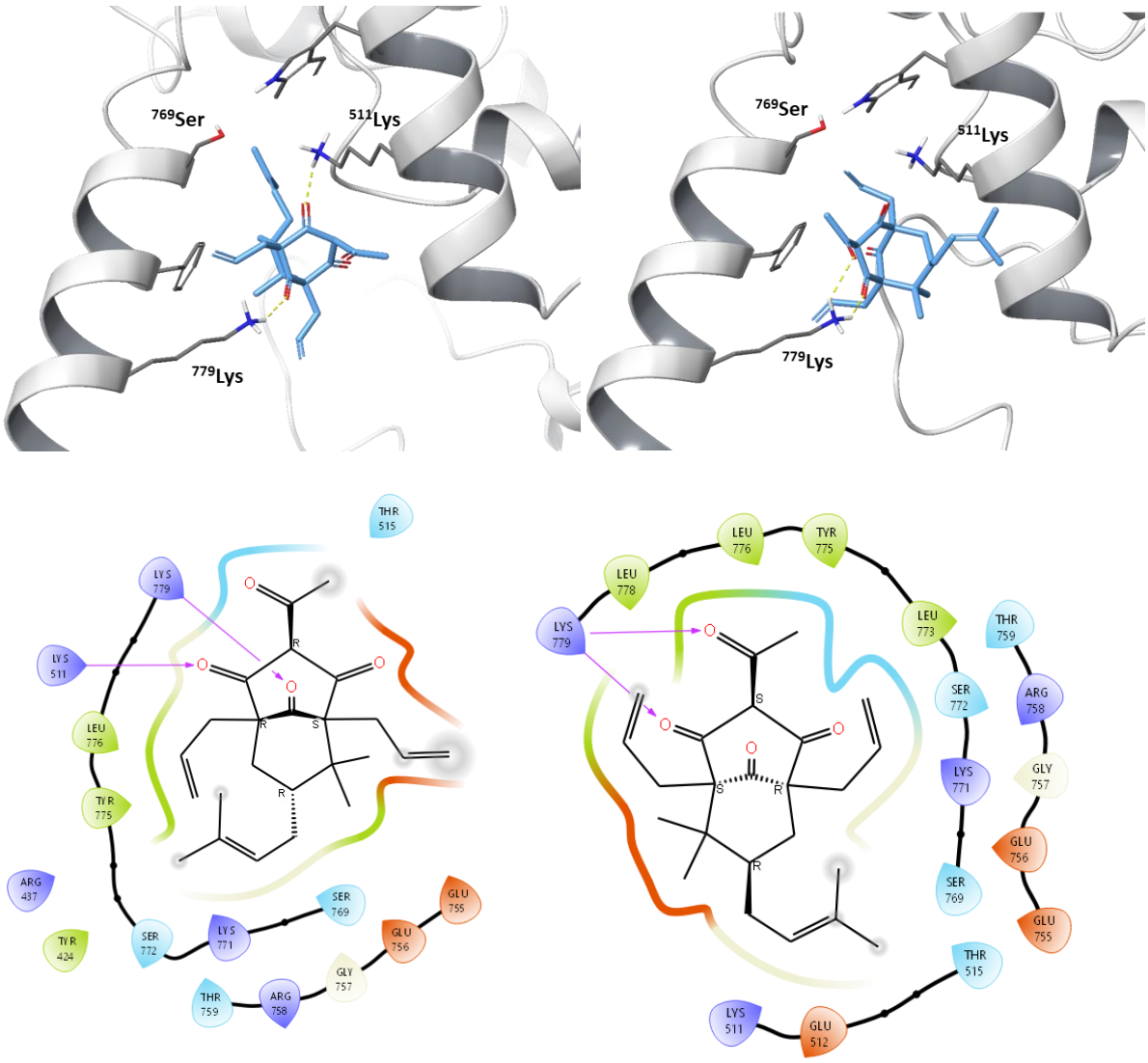

SI Figure 9 Binding mode of both PPAP53 isomers (blue) within RT-TRPC6 (white) with corresponding 2D ligand interaction diagram. The violet lines indicate hydrogen bond interactions. The polar and hydrophobic residues are highlighted in blue and green, positive and negative charged residues are highlighted in purple and red respectively.

2.4 Binding mode of Hyperforin in RT-TRPC6

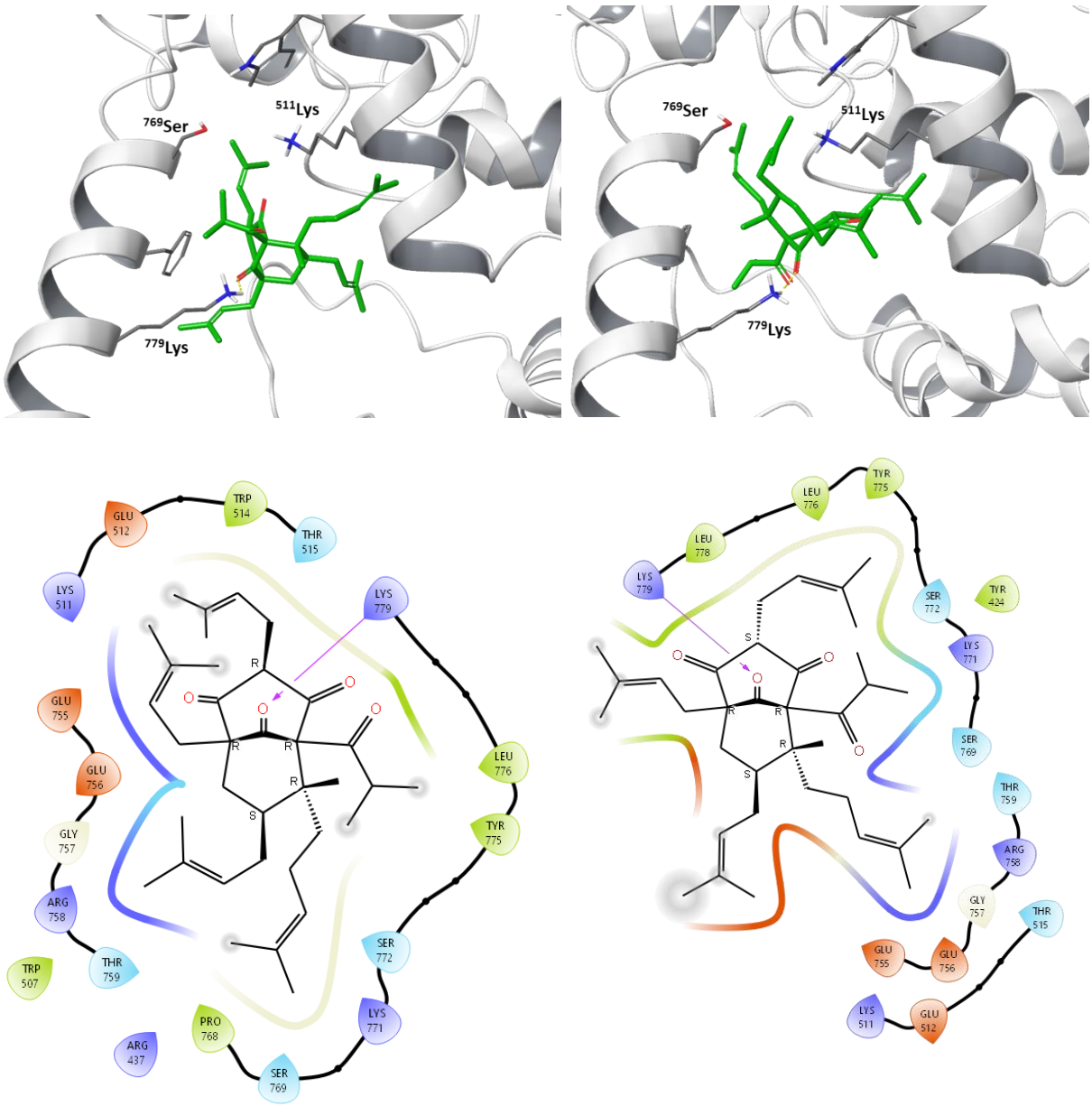

SI Figure 10 Binding mode of both hyperforin isomers (green) within RT-TRPC6 (white) with corresponding 2D ligand interaction diagram. The violet lines indicate hydrogen bond interactions. The polar and hydrophobic residues are highlighted in blue and green, positive and negative charged residues are highlighted in purple and red respectively.

3. SIFt calculation

3.1 SIFt PPAP53 in RT-TRPC6 – all interactions

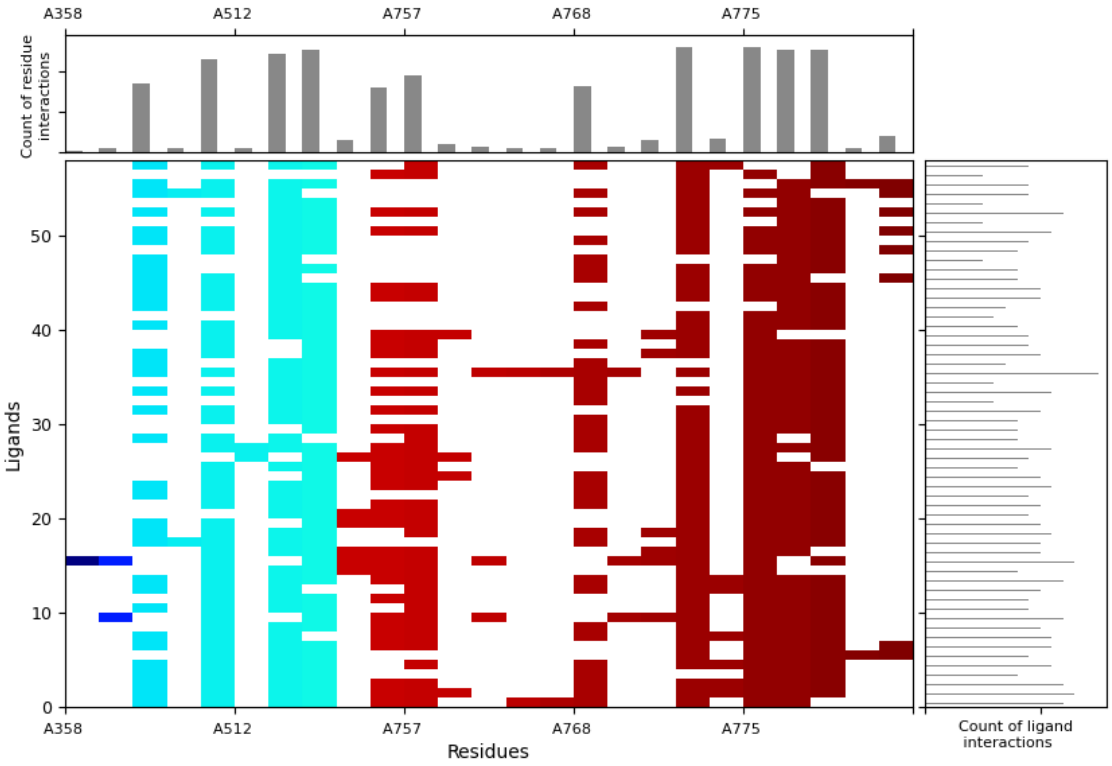

3.2 SIFt PPAP53 in RT-TRPC6 –hydrogen bond donor residues

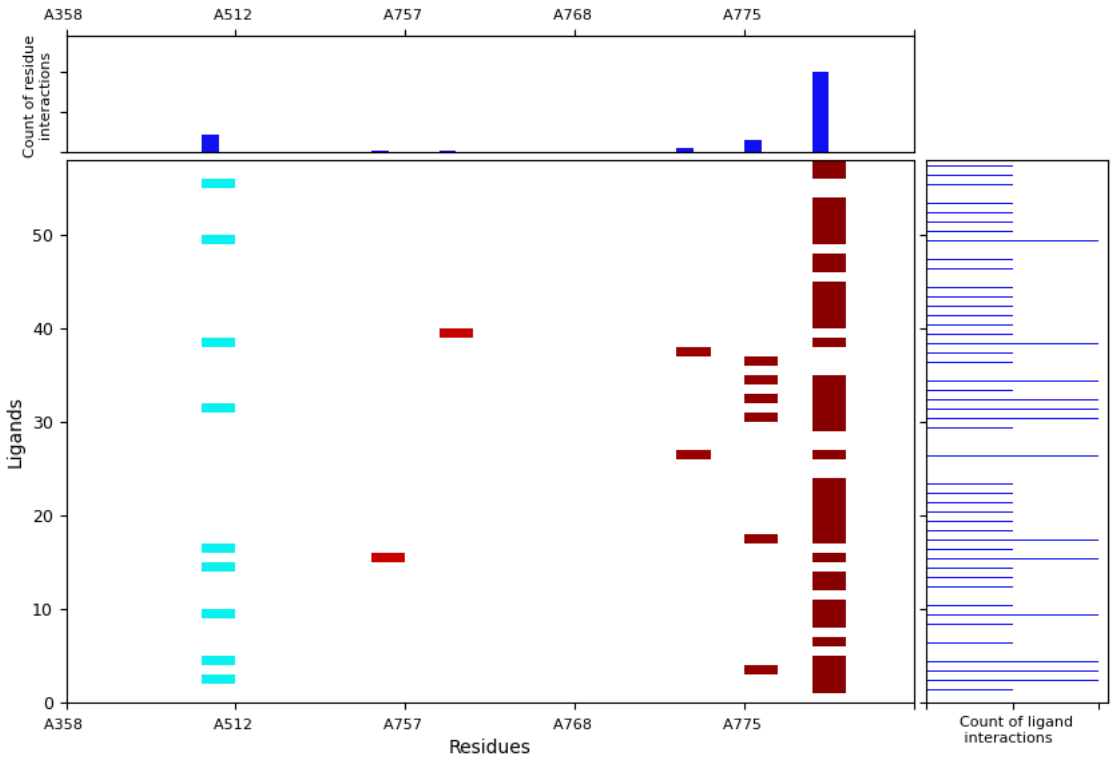

3.3 SIFt PPAP53 in RT-TRPC6 –hydrogen bond acceptor residues

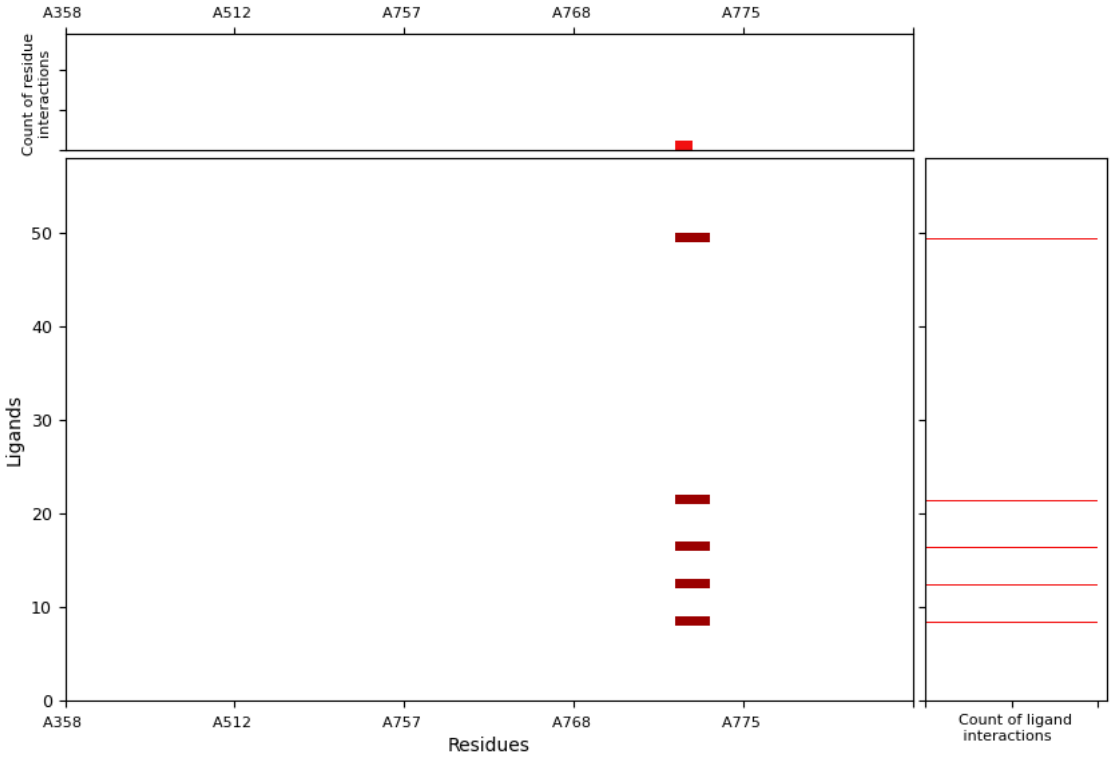

3.4 SIFt PPAP53 in RT-TRPC6 –backbone residues

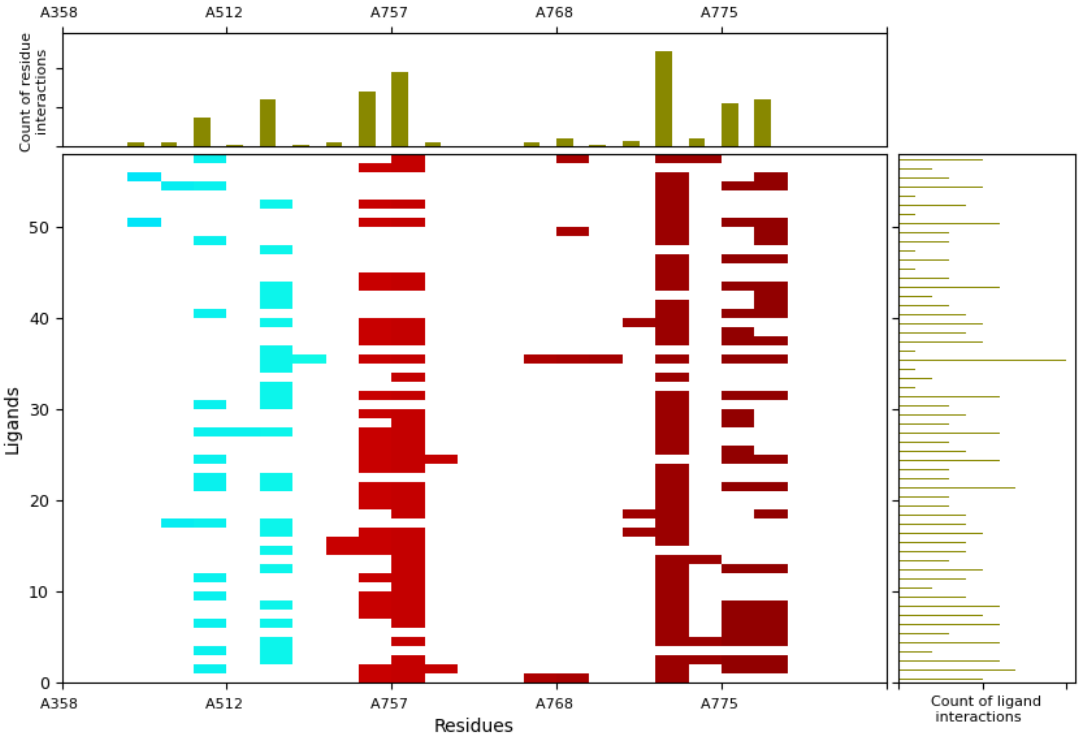

3.5 SIFt PPAP53 in RT-TRPC6 –charged residues

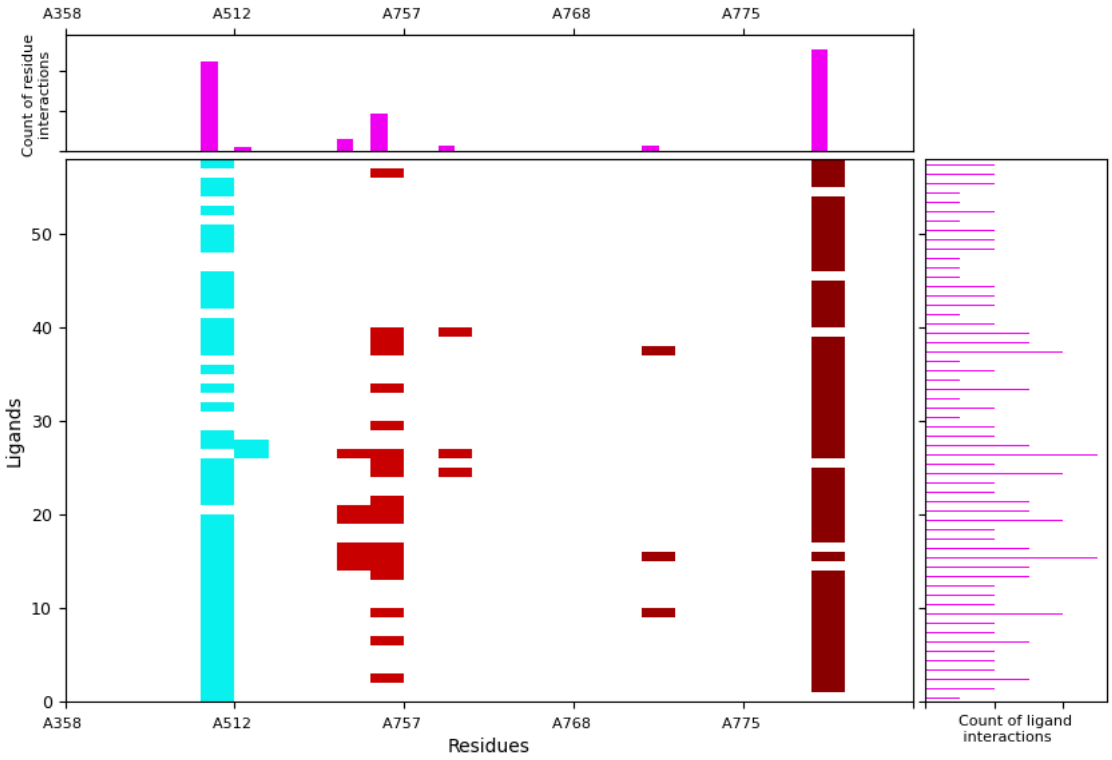

3.6 SIFt PPAP53 in RT-TRPC6 –aromatic residues

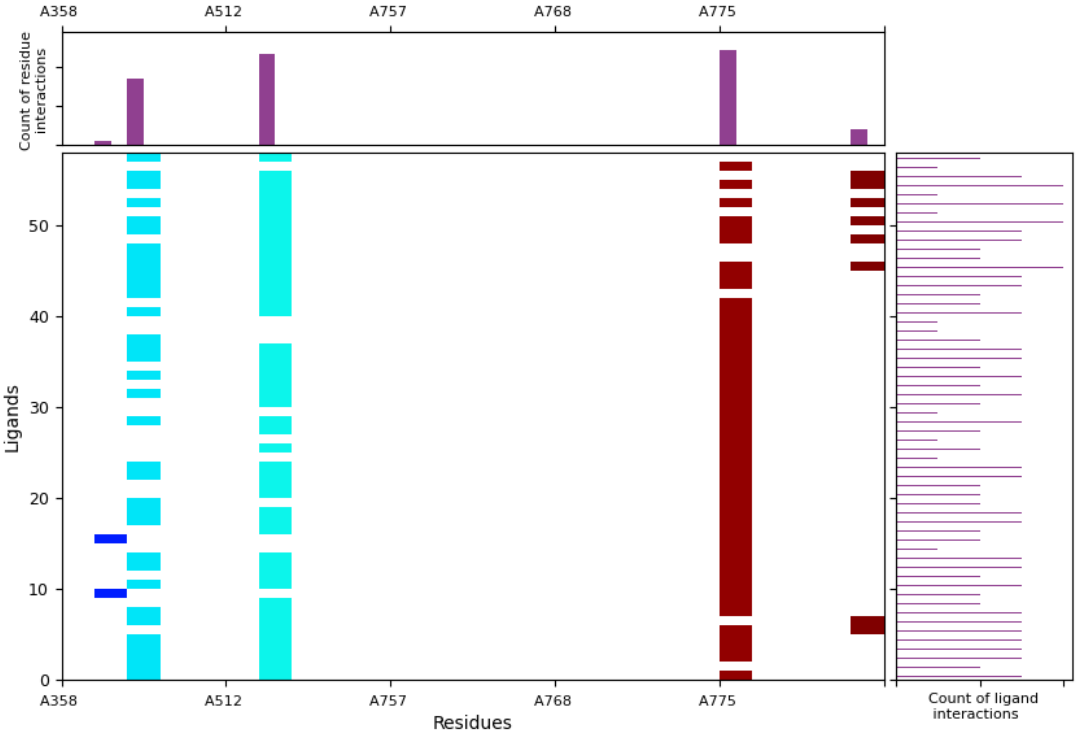

3.7 SIFt PPAP53 in RT-TRPC6 –polar residues

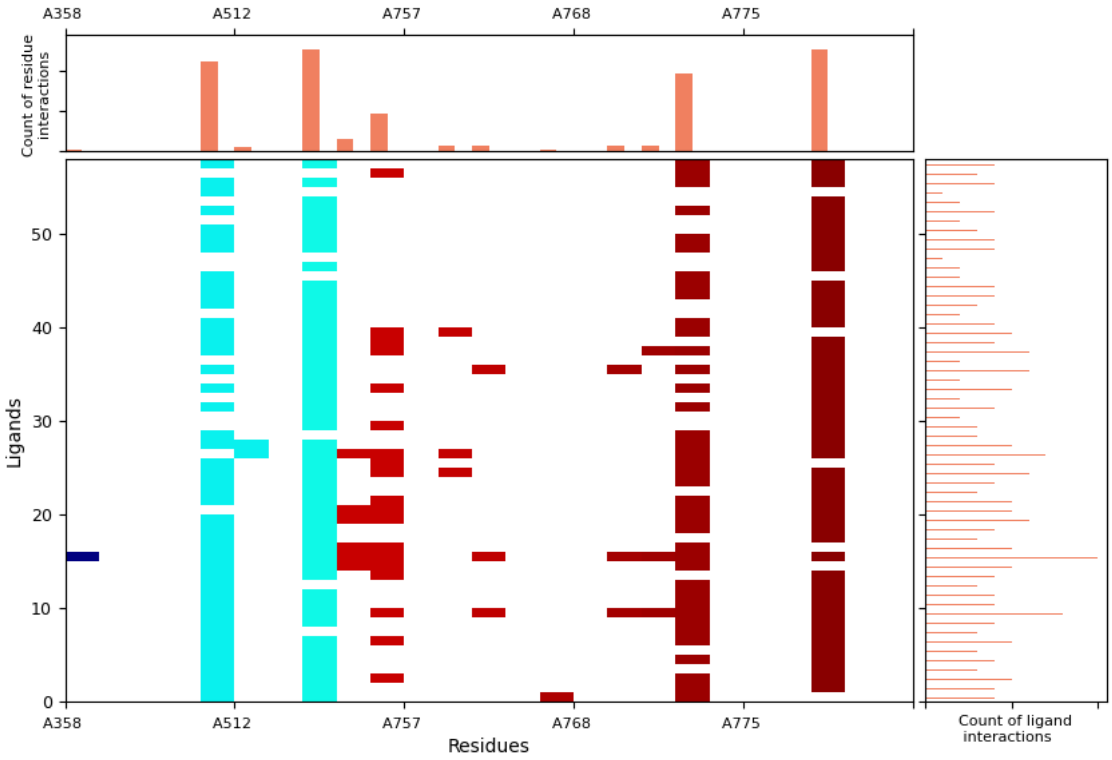

3.8 SIFt PPAP53 in RT-TRPC6 –sidechain residues

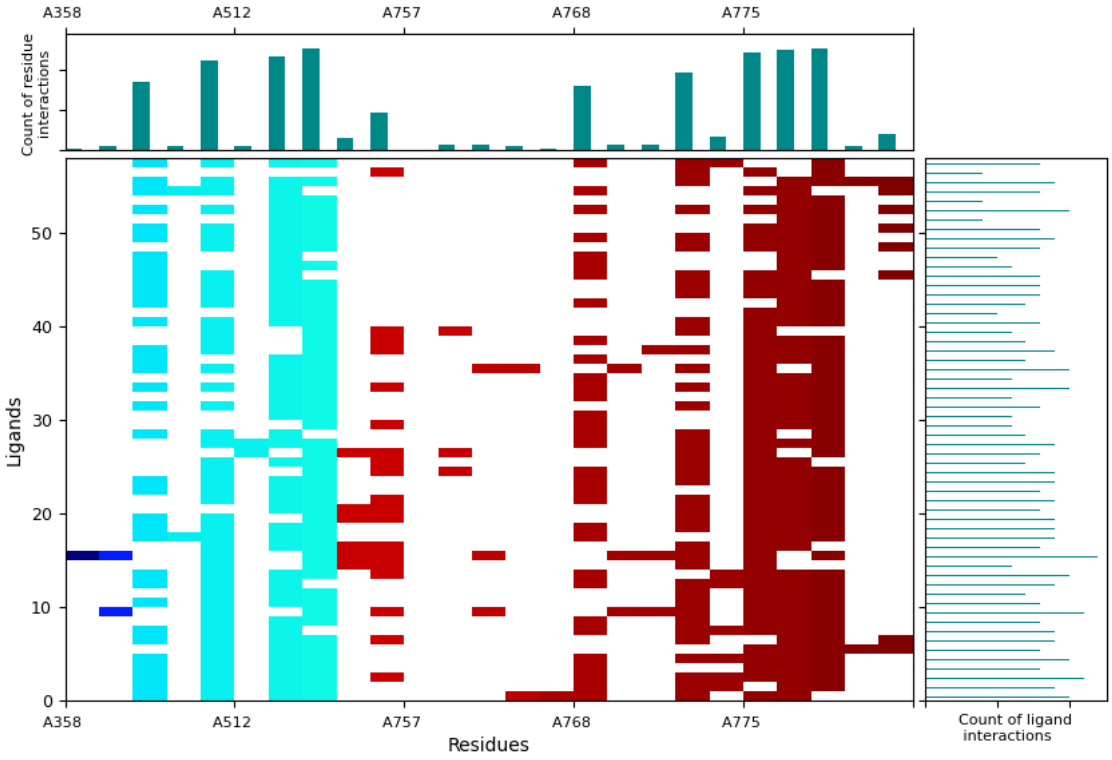

3.9 SIFt PPAP53 in RT-TRPC6 –hydrophobic residues

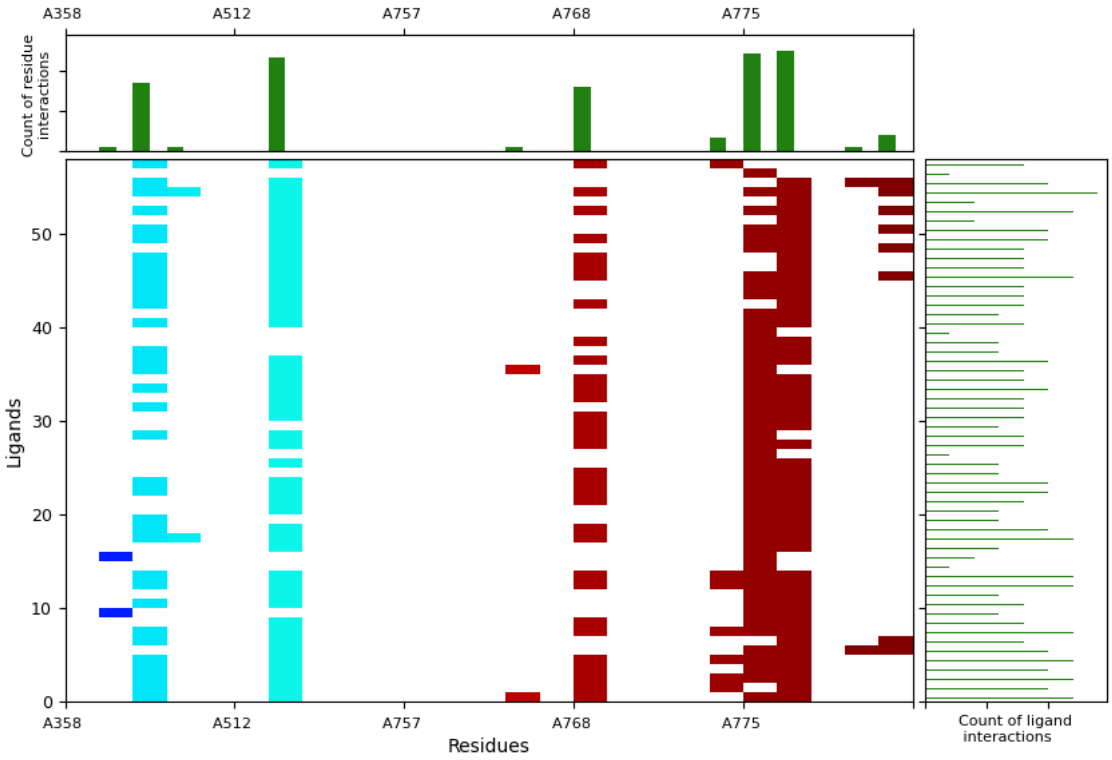

4. ^{1}H- and ^{13}C-NMR

4.1 Compound PPAP53

^{1}H-NMR (300 MHz, D_2O)

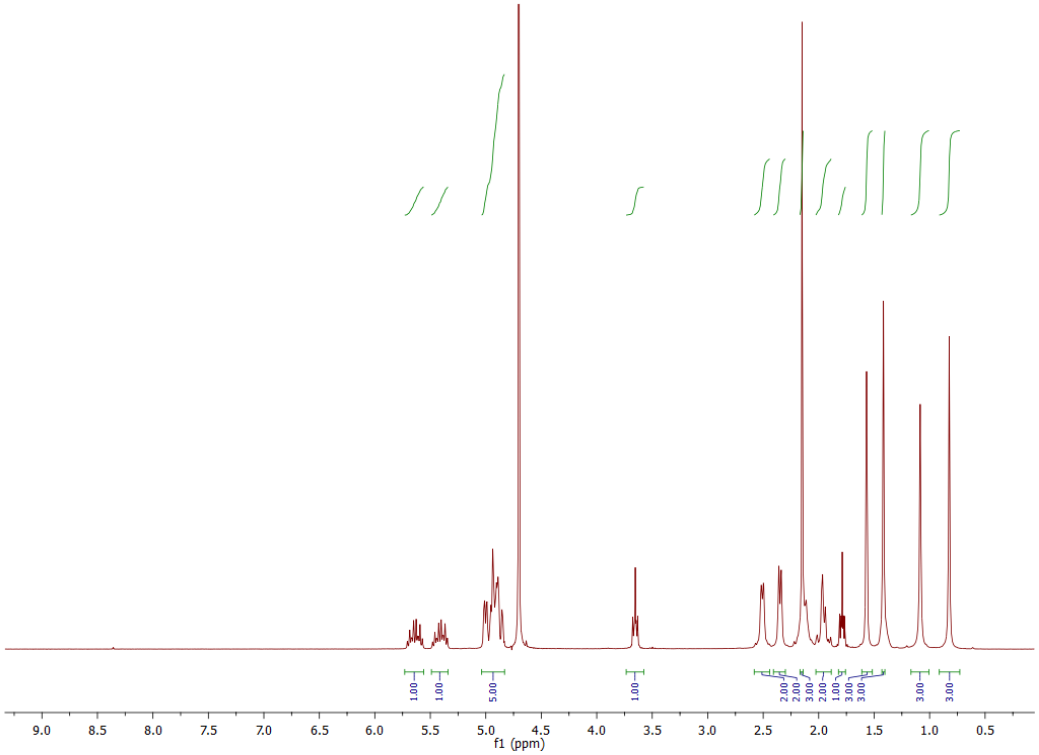

^{13}C-NMR (151 MHz, D_2O)

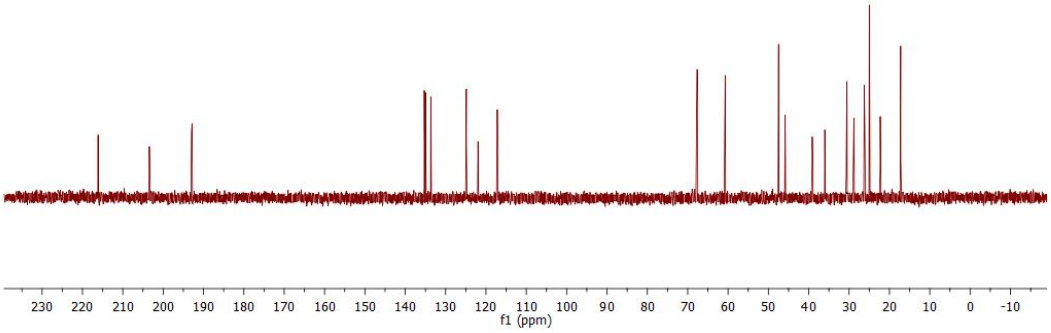

4.2 Compound PPAP61

^{1}H-NMR (300 MHz, D_2O)

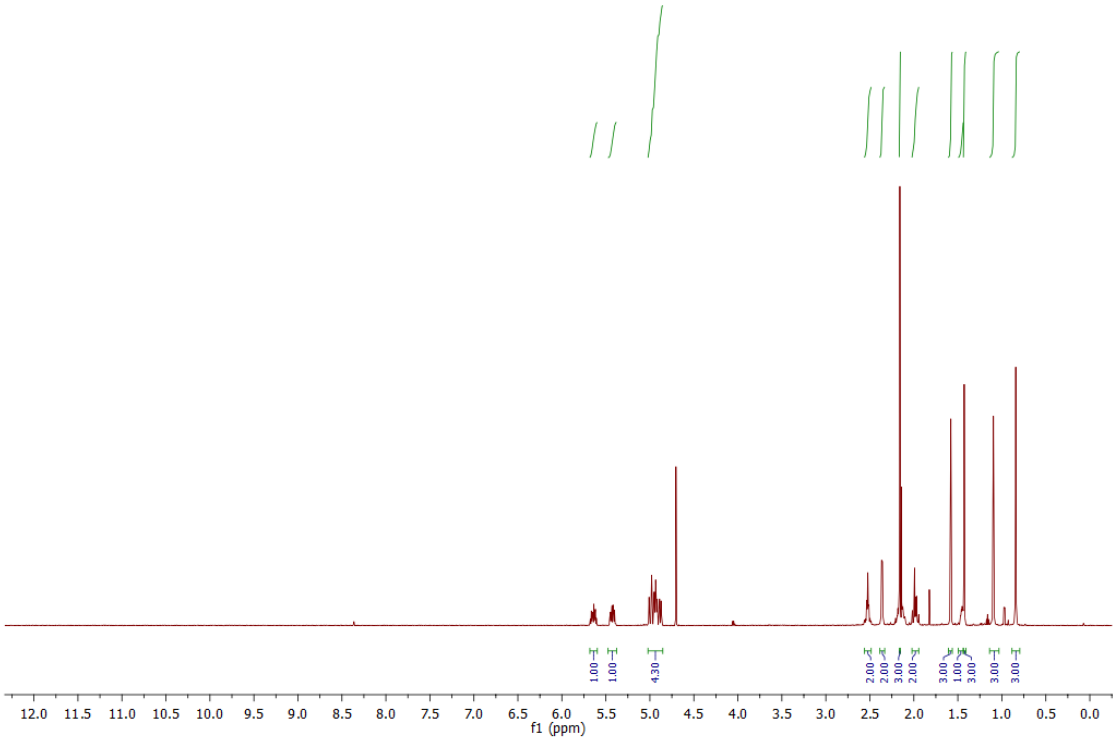

^{13}C-NMR (151 MHz, DMSO-d_6)

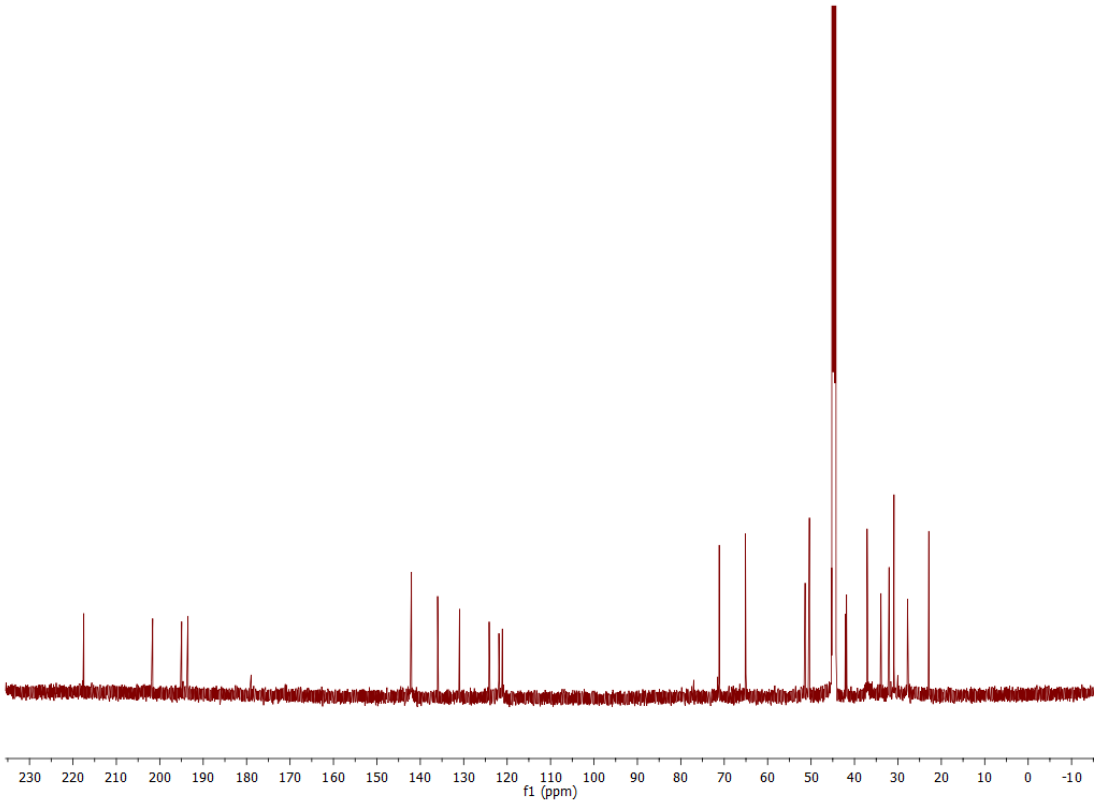

4.3 Compound PPAP60

^{1}H-NMR (300 MHz, MeOD)

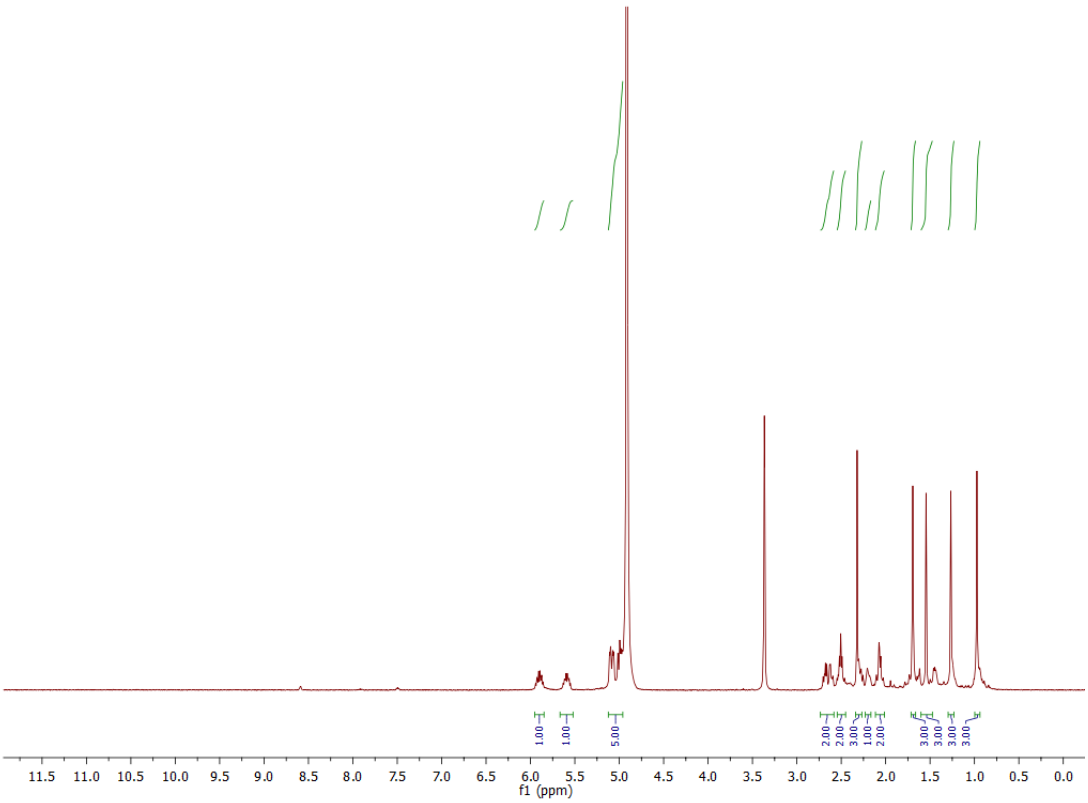

^{13}C-NMR (151 MHz, DMSO-d_6)

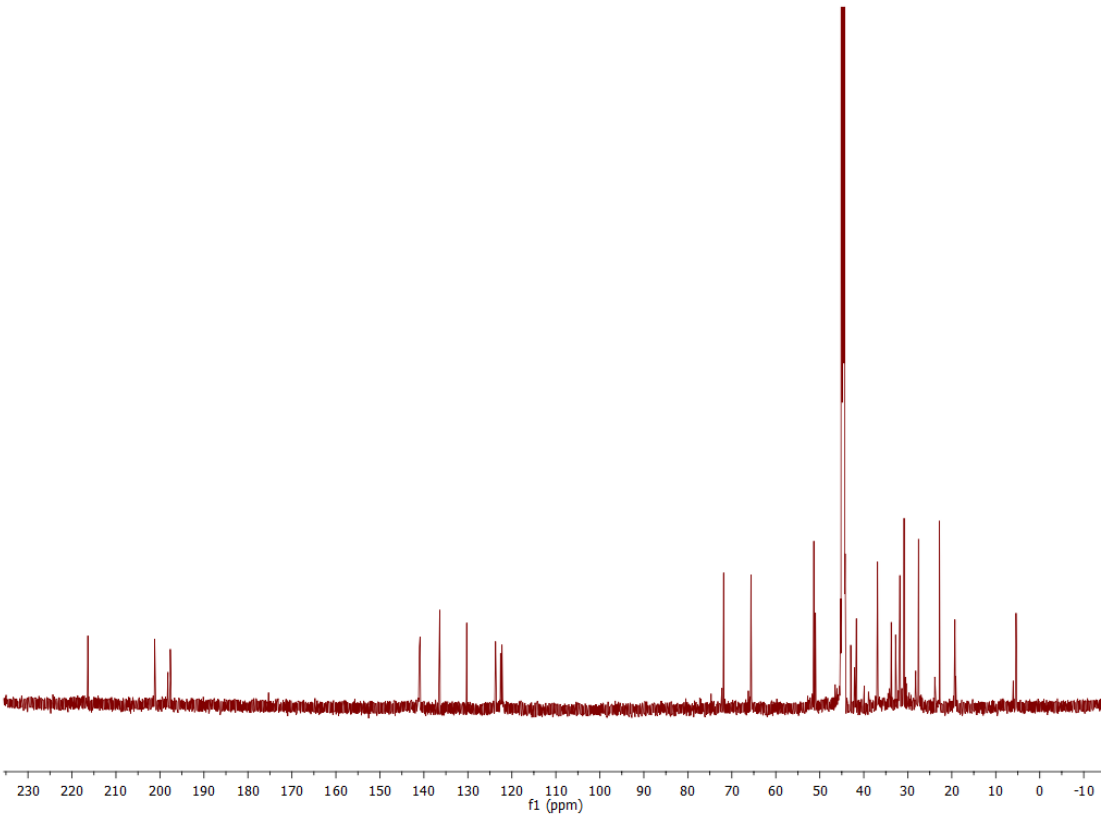

4.4 Compound PPAP57

^{1}H-NMR (300 MHz, D_2O)

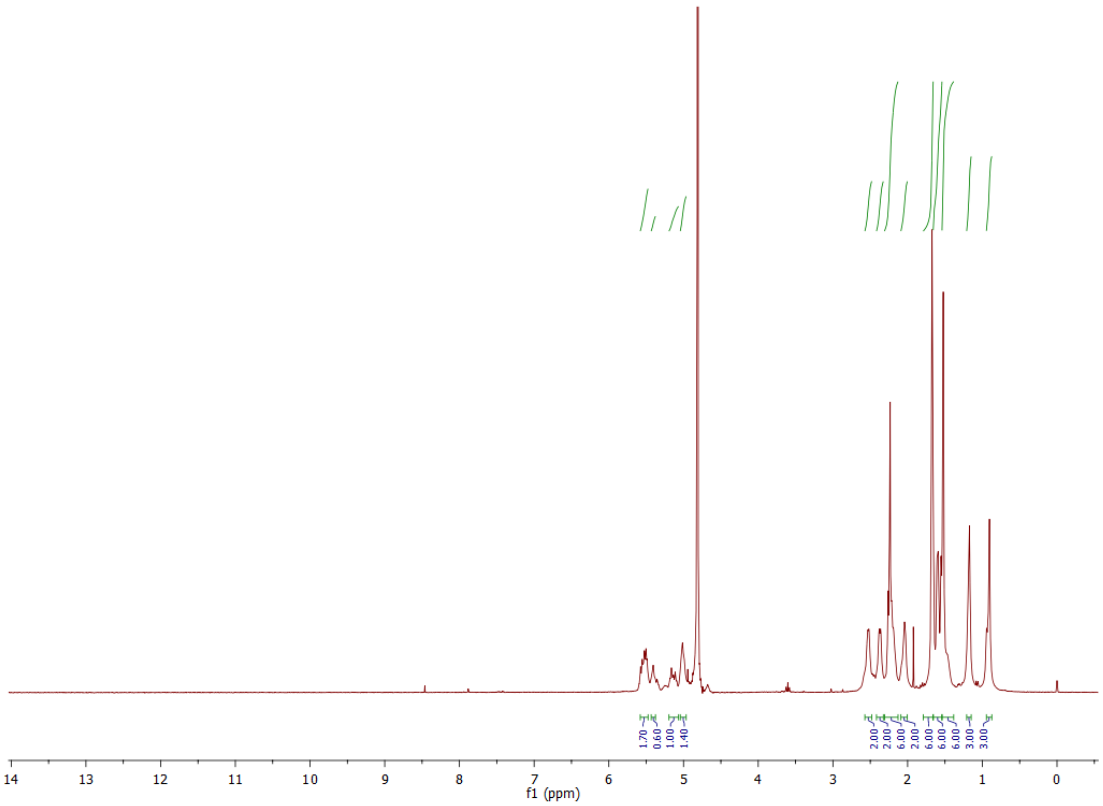

^{13}C-NMR (151 MHz, D_2O)